We are IntechOpen, the world's leading publisher of Open Access books
Built by scientists, for scientists

4,800
Open access books available

122,000
International authors and editors

135M
Downloads

Our authors are among the

154
Countries delivered to

TOP 1%
most cited scientists

12.2%
Contributors from top 500 universities

WEB OF SCIENCE™

Selection of our books indexed in the Book Citation Index in Web of Science™ Core Collection (BKCI)

Interested in publishing with us?
Contact book.department@intechopen.com

Numbers displayed above are based on latest data collected.
For more information visit www.intechopen.com

14

Integrated Vehicle Health Management for Solid Rocket Motors

D.G. Luchinsky[1,2], V.V. Osipov[1,2], V.N. Smelyanskiy[1], I. Kulikov[1], A. Patterson-Hein[1], B. Hayashida[3], M. Watson[3], D. Shook[4], M. Johnson[4], S. Hyde[4] and J. Shipley[4]

[1]*NASA Ames Research Center, MS 269-3, Moffett Field, CA, 94035,*
[2]*Mission Critical Technologies Inc., 2041 Rosecrans Ave., Suite 225 El Segundo, CA 90245,*
[3]*ISHM and Sensors Branch, NASA Marshall Space Flight Center, Huntsville, Alabama 35812,*
[4]*ATK Thiokol Launch Systems R&D Labs, Large Salt Lake City Area, Utah, USA*

1. Introduction

Solid rocket motors (SRMs) are an integral part of human space flight providing a reliable means of breaking away from the Earth's gravitational pull. The development and deployment of an integrated system health management (ISHM) approach for the SRMs is therefore a prerequisite for the safe exploration of space with the next-generation Crew and Heavy-Lift Launch Vehicles. This unique innovative technological effort is an essential part of the novel safety strategy adopted by NASA.

At the core of an on-board ISHM approach for SRMs are the real-time failure detection and prognostics (FD&P) technique. Several facts render the SRMs unique for the purposes of FD&P: (i) internal hydrodynamics of SRMs is highly nonlinear, (ii) there is a number of failure modes that may lead to abrupt changes of SRMs parameters, (iii) the number and type of sensors available on-board are severely limited for detection of many of the main SRM failure modes; (iv) recovery from many of the failure modes is impossible, with the only available resource being a limited thrust vector control authority (TVC); (iii) the safe time window between the detectable onset of a fault and a possible catastrophic failure is very short (typically a few seconds). The overarching goal of SRM FD&P is to extract an information from available data with precise timing and a highest reliability with no "misses" and no "false alarms". In order to achieve this goal in the face of sparse data and short event horizons, we are developing: (i) effective models of nominal and off-nominal SRM operation, learned from high-fidelity simulations and firing tests and (ii) a Bayesian sensor-fusion framework for estimating and tracking the state of a nonlinear stochastic dynamical system. We expect that the combination of these two capabilities will enable in-flight (real time) FD&P.

Source: Aerospace Technologies Advancements, Book edited by: Dr. Thawar T. Arif,
ISBN 978-953-7619-96-1, pp. 492, January 2010, INTECH, Croatia, downloaded from SCIYO.COM

Indeed, dynamical models of internal SRMs ballistics and many SRMs fault modes are well studied, see e.g. (Culick, 1996; Salita, 1989; Sorkin, 1967) and references therein. Examples of faults, for which quite accurate dynamical models can be introduced, include: (1) combustion instability; (ii) case breach fault, i.e. local burning-through of the rocket case; (iii) propellant cracking; (iv) overpressure and breakage of the case induced by nozzle blocking or bore choking. The combustion instabilities were studied in detail in the classical papers of (Culick & Yang, 1992; Culick, 1996) and (Flandro et al, 2004). Bore choking phenomenon due to radial deformation of the propellant grain near booster joint segments was studied numerically in (Dick et al., 2005; Isaac & Iverson, 2003; Wang et al., 2005) and observed in primary construction of the Titan IV (see the report, Wilson at al., 1992).

The FD&P system can be developed using the fact that many fault modes of the SRMs have unique dynamical features in the time-traces of gas pressure, accelerometer data, and dynamics of nozzle gimbal angle. Indeed, analysis shows that many fault modes leading to SRMs failures, including combustion instabilities (Culick,1974; Culick & Yang, 1992; Culick,1996; Flandro et al, 2004), bore choking (Dick et al., 2005; Isaac & Iverson, 2003; Wang et al., 2005), propellant cracking, nozzle blocking, and case breach (Rogers, 1986), have unique dynamical features in the time-traces of pressure and thrust. Ideally, the corresponding expert knowledge could be incorporated into on-board FD&P within a general Bayesian inferential framework allowing for faster and more reliable identification of the off-nominal regimes of SRMs operation in real time. In practice, however, the development of such an inferential framework is a highly nontrivial task since the internal ballistics of the SRMs results from interplay of a number of complex nonlinear dynamical phenomena in the propellant, insulator, and metal surfaces, and gas flow in the combustion chamber and the nozzle. On-board FD&P, on the other hand, can only incorporate low-dimensional models (LDMs) of the internal ballistics of SRMs. The derivation of the corresponding LDMs and their verification and validation using high-fidelity simulations and firing tests become an essential part of the development of the FD&P system.

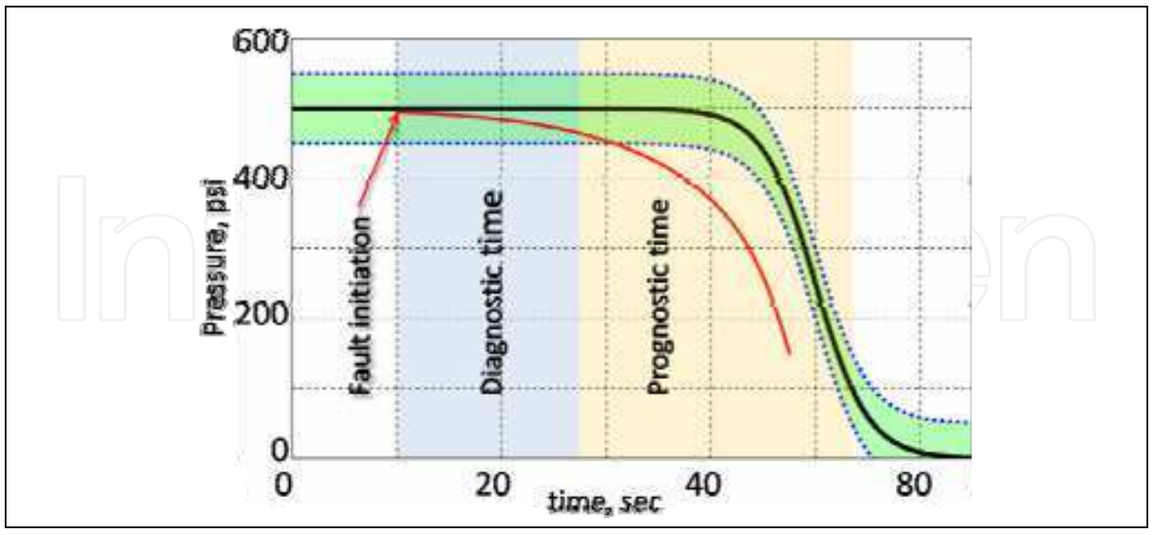

Fig. 1. Typical time-trace of pressure in the nominal regime is shown by the black line with pressure safety margins indicated by the green shading region. Fault-induced pressure time-trace in off-nominal regime is shown by the red line. Blue shading indicates diagnostic window and yellow shading indicates prognostic window.

At present the FD&P system in SRMs involves continuous monitoring of the time-traces of such variables as e.g. pressure, thrust, and altitude and setting up conservative margins on the deviation of these variables from their nominal values (see schematics in Fig. 1). However, in the absence of the on-board FD&P analysis of the SRM performance the probability of "misses" and "false alarms" is relatively high and reliability of the IVHM is reduced (see e.g. Rogers, 1986; Oberg, 2005). The goal of the on-board FD&P will be to detect the initiation time of the fault and provide its continuous diagnostic and prognostic while the performance variables are still within the safety margins to support the decision and to reduce the probability of "misses" and "false alarms".

In this chapter we report the progress in the development of such FD&P system. The main focus of our research was on the development of the: (i) model of internal ballistics of large segmented SRMs in the nominal regime and in the presence of number of fault modes including first of all case breach fault; (ii) model of the case breach fault; (iii) algorithms of the diagnostic and prognostic of the case breach fault within a general inferential Bayesian framework; and (iv) verification and validation of these models and algorithms using high-fidelity simulations and ground firing tests.

The chapter is organized as follows. In the next section we describe the low-dimensional performance model of internal ballistics of the SRMs in the presence of faults. In the Sec. III we modify this model for a subscale solid motor, analyze the axial distributions and validate the results of this model based on high-fidelity FLUENT simulations and analysis of the results of a ground firing test of the sub-scale motor faults. Developed Bayesian inferential framework for the internal SRM ballistics and FD&P algorithms is presented in the Sec. IV. FD&P for large segmented SRMs is analyzed in the Sec. V. Finally, in the Conclusions we review the results and discuss a possibility of extending proposed approach to an analysis of different faults.

2. Internal ballistics of the SRMs

The internal ballistics of the SRMs in the presence of the fault can be conveniently described by the following set of stochastic partial differential equations representing conservation laws for mass, momentum, and energy of the gas (Sorkin, 2005; Culick & Yang, 1992; Salita, 1989 & 2001)

$$\partial_t \left(U A_p \right) + \partial_x \left(f(U) A_p \right) = S, \tag{1}$$

where conservative variables of the gas dynamics and function $f(U)$ are given by the following equations

$$U = \begin{bmatrix} \rho \\ \rho u \\ \rho e_T \end{bmatrix}, \quad f(U) = \begin{bmatrix} \rho u \\ \rho u^2 + p \\ \rho u e_T + up \end{bmatrix}, \tag{2}$$

$e_T = c_V T + u^2/2$, $h_T = c_p T + u^2/2$, are the total energy and total enthalpy of the gas flow, $H = c_p T_0$ is the combustion heat of solid propellant and the source terms that include fault terms at a given location x_0 have the form

$$S=\begin{bmatrix} \rho_p \dot{R} l(x) - \rho_{t,h} u_{t,h} A_h \delta(x-x_0) + \xi_1(t) \\ p\partial_x A_p - \lambda \rho u^2 l(x) + \xi_2(t) \\ H\rho_p \dot{R} l(x) - h_{t,h} \rho_{t,h} u_{t,h} A_h \delta(x-x_0) + \xi_3(t) \end{bmatrix}. \quad (3)$$

This model extends the previous work (Salita, 1989 & 2001) in a number of important directions. To model various uncontrollable sources of noise (such as cracks and case vibrations) that may become essential in off-nominal conditions and may screen the variation of the system parameters a random component in the propellant density $\rho_p \rightarrow \rho_p[1+\sqrt{\sigma}\cdot\xi(t)]$ is introduced. Various faults can be modeled within the set of Eqs. (1)-(3) (including nozzle failure, propellant cracking, bore choking, and case breach) by choosing the time scale and direction of the geometrical alternations of the grain and case and the corresponding form of the sourse/sink terms. In particular, for the case breach fault two additional terms in the 1st and 3rd equations in Eqs. (3) correspond to the mass and energy flow from the combustion chamber through the hole in the rocket case with cross-section area $A_h(t)$. We now extend this mode by coupling the gas dynamics in the combustion chamber to the gas flow in the hole. The corresponding set of PDEs

$$\begin{cases} \partial_t (A_h \rho_h) = -\partial_x (A_h \rho_h u_h), \\ \partial_t (A_h \rho_h u_h) = -\partial_x (A_h \rho_h u_h^2) - A_h \partial_x p_h - f_{fr} l_h, \\ \partial_t (A_h \rho_h e_{t,h}) = -\partial_x \left[A_h \rho_h u_h h_{t,h} \right] - Q_h l_h, \end{cases} \quad (4)$$

resembles Eqs. (1). The important difference, however, is that we neglect mass flow from the walls of the hole. Instead Eqs. (4) include the term that describes the heat flow from the gas to the hole walls. The boundary conditions for this set of equations assume ambient conditions at the hole outlet and the continuity equation for the gas flow in the hole coupled to the sonic condition at the hole throat. The value of Q_h is presented in Eq. (14). The dynamics of the gas flow in the nozzle is described by a set of equations similar to (4) and can be obtained from this set by substituting subscript "n" for subscript "h".

The model (1)-(4) allow us to include possible burning rate variations and also various uncontrolled sources of noise, such as grain cracks and case vibrations to simulate more realistic time-series data representing off-nominal SRM operation. Due to the high temperature T of combustion products in the combustion chamber, the hot mixed gas can be considered as a combination of ideal gases. As we are interested in average gas characteristics (head pressure and temperature) we will characterize the combustion products by averaged parameters using the state equation for an ideal gas:

$$\frac{p}{\rho} = (c_P - c_V)T = \frac{p_0}{\rho_0}\left(\frac{T}{T_0}\right) = \frac{c_0^2}{\gamma}\left(\frac{T}{T_0}\right) \quad (5)$$

2.1 Regression of propellant surface

We take into account the propellant erosion in a large segmented rocket assuming that the erosive burning rate can be presented in the form

$$\dot{R} = r_b = ap^n + \dot{r}_{er}. \quad (6)$$

The erosive burning is taken into account in the Vilyunov's approximation

$$\dot{r}_{er} = C\left(I - I_{cr}\right) \tag{7}$$

for $I > I_{cr}$ and 0 otherwise, where C and I_{cr} are constants and I=const$(\rho u / r_b \rho_p)$Re$^{-1/8}$, where Re is the Reynolds number.

2.2 Model of the propellant geometry

To model the actual propellant geometry along the rocket axis the combustion chamber is divided into N segments as schematically shown in the Fig. 2. For each ballistic element the port area $A_p(x_i)$ and perimeter $l(x_i)$ averaged over the segment length dx_i are provided in the form of the design curves

$$A_p(x_i) = f_{Ai}(R(x_i)), \quad l(x_i) = f_{li}(R(x_i)) \tag{8}$$

(see Fig. 2). Note that the burning area and the port volume for each segment are given by the following relations

$$dV(x_i) = A_b(x_i)dx_i, \quad dA_b(x_i) = l(x_i)dx_i, \tag{9}$$

and, therefore, are uniquely determined by the burning rate r_{bi} for each ballistic element.
For numerical integration each segment was divided into a finite number of ballistic elements. The design curves were provided for each ballistic segment.

2.3 Model of the nozzle ablation

To model nozzle ablation we use Bartz' approximation (Bartz, 1965; Hill and Peterson,1992; Handbook, 1973) for the model of the nozzle ablation (Osipov et al., March 2007, and July 2007; Luchinsky et al., 2007) in the form:

$$\begin{aligned} \dot{R}_N &= v_{t0}\left(p / p_{\max}\right)^{1-\beta}\left(R_N / R_{t,in}\right)^{-\beta}\left[\left(T - T_{abl}\right)/\left(T_t - T_{abl}\right)\right], \\ v_{t0} &= \varepsilon C_p\left(\frac{\gamma p_{\max}}{\Gamma c_0}\right)^{1-\beta}\left(\frac{2R_{t,in}}{\mu}\right)^{-\beta}\frac{\left(T_t - T_{abl}\right)}{\left[c_{ins}\left(T_{abl} - T_0\right) + q_{ins}\right]}, \end{aligned} \tag{10}$$

where $\beta \approx 0.2$ and $\varepsilon \approx 0.023$. In a particular case of the ablation of the nozzle throat and nozzle exit this approximation is reduced to

$$\dot{R}_t = v_{m,t}\left(\frac{p_0}{p_{\max}}\right)^{1-\beta}\left(\frac{R_t}{R_{t,in}}\right)^{-\beta}, \quad A_t(t) = \pi R_t^2(t), \tag{11}$$

$$\dot{R}_{ex} = v_{m,ex}\left(\frac{p_0 A_t}{p_{\max} A_{ex}}\right)^{1-\beta}\left(\frac{R_{ex}}{R_{ex,in}}\right)^{-\beta}\frac{\left(T_{ex} - T_{abl}\right)}{\left(T_t - T_{abl}\right)}, \tag{12}$$

where $R_{t,in}$=$R_t(0)$, $R_{ex,in}$=$R_{ex}(0)$ and $v_{m,t}$ and $v_{m,ex}$ are experimentally determined constants. In practice, to fit experimental or numerical results on the nozzle ablation it suffice to put β = 0.2 and to obtain values of $v_{m,t}$ and $v_{m,ex}$ by regression.

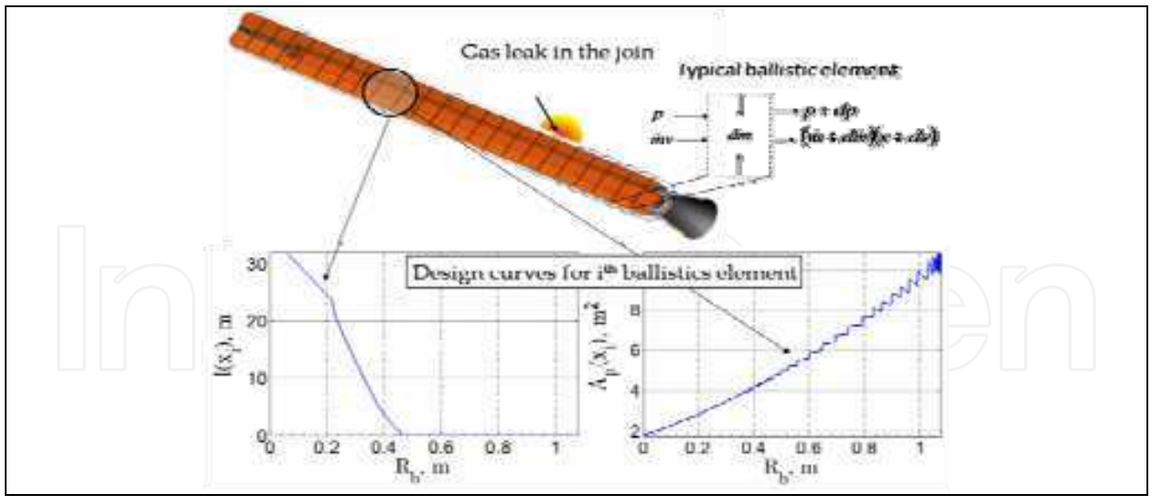

Fig. 2. Sketch of a cross-section of an idealized geometry of the multi-segment RSRMV rocket and an example of the design curves (8) for the head section.

2.4 Model of the burning-though of a hole

To complete the model of the case breach fault for the segmented SRMs the system of equations (1)—(12) above has to be extended by including equations of the hole growth model (Osipov et al., 2007, March and 2007, July; Luchinsky et al., 2007)

$$\dot{R}_h = v_h(p_{t,h}, T_{h,t}) = \frac{Q_c + Q_R + Q_b}{\left[q_{met} + C_{met}\left(T_{mel} - T_{m0}\right)\right]\rho_{met}}, \tag{13}$$

$$\begin{aligned} Q_R &= \sigma\left[1 - \exp\left(-\lambda p_{t,h}\right)\right]\left(T_t^4 - T_{met}^4\right), \\ Q_c &= 0.023 C_p \left(\frac{\gamma p_{t,h}}{\Gamma c_0}\right)^{0.8} \left(\frac{2R_h}{\mu}\right)^{-0.2} \left(T_t - T_{met}\right), \\ Q_b &= v_{fb}\left[q_{met} + C_{met}\left(T_{mel} - T_{m0}\right)\right]\rho_{met}. \end{aligned} \tag{14}$$

Here $Q_h = Q_c + Q_R + Q_b$.

3. A subscale motor

Motivated by the results of the ground firing test let us consider an application of the model (1)-(14) to an analysis of the case breach fault in a subscale motor. Note that a subscale motor can be consider as model (1)-(14) consisting of one ballistic element. In this case the velocity of the flow is small and one can neglect the effects of erosive burning, surface friction, and the variation of the port area along the motor axis.

3.1 SRM internal ballistics in the "filling volume" approximation

To derive the LDM of the case breach fault we integrate equations (1) along the rocket axis and obtain the following set of ordinary differential equations for the stagnation values of the gas parameters and the thickness of the burned propellant layer

$$\begin{cases} \partial_t\left(\rho_0 V\right) = -\left(\rho u A\right)\big|_L + \rho_p r_b(p_0) A_b + A_1\xi_1(t), \\ \partial_t\left(\rho_0 e_0 V\right) = -\left(\rho u A h_t\right)\big|_L + H\rho_p r_b(p_0) A_b + A_2\xi_2(t), \\ \partial_t R = r_b\left(p_0\right). \end{cases} \tag{15}$$

Here $(\rho uA)\,|_L$ and $(\rho uAh_t)\,|_L$ are the mass and the enthalpy flow from the whole burning area of the propellant including the propellant surface in the hole and p_0, ρ_0, and e_0 are the stagnation values of the flow parameters. The total mass flow from the burning propellant surface is equal to the sum of the mass flows through the nozzle' and hole throats. Assuming that sonic conditions hold both in the nozzle throat and the hole throat we obtain the following result

$$\begin{aligned} &\left(\rho uA\right)\big|_L = \left(\rho_h u_h A_h\right)\big|_t + \left(\rho uA\right)\big|_t = \\ &\quad \Gamma^{-1}\sqrt{\gamma\rho_0 p_0}\,A_{t,h} + \Gamma^{-1}\sqrt{\gamma\rho_0 p_0}\,A_t = \Gamma^{-1}\sqrt{\gamma\rho_0 p_0}\left(A_{t,h} + A_t\right) \end{aligned} \tag{16}$$

Here $\Gamma=((\gamma+1)/2)^{(\gamma+1)/2(\gamma-1)}$ and $A_{et}=(A_{t,h}+A_t)$ is the effective nozzle throat area. This relation means that in the first approximation the hole is seen by the internal flow dynamics as an increase of the nozzle throat area and the dynamics of the stagnation values of the gas parameters are governed by both dynamics of the propellant burning area (related to the thickness of the burned propellant layer R) and by the hole radius R_h. Substituting results of integration (16) into (15) and using model for nozzle ablation (11), (12) and hole melting (13), (14) we obtain the low-dimensional model of the internal ballistic of a subscale SRM in the presence of the case breach fault in the form

$$\begin{aligned} &\dot\rho = -\frac{c_0\Gamma A_{et}}{V r_b}\rho\sqrt{\frac{p}{\rho}} + \frac{A_b}{V}\left(\rho_p - \rho\right)p^n + a_1\xi_1(t), \\ &\dot p = -\frac{c_0\gamma\Gamma A_{et}}{V r_b}p\sqrt{\frac{p}{\rho}} + \frac{A_b}{V}\left(\gamma\rho_p - p\right)p^n + a_2\xi_2(t), \\ &\dot R = r_b p^n, \quad A_b = f(R), \quad \dot V = A_b\dot R = f(R) r_b p^n, \\ &\dot R_t = v_{abl} = v_m\left(\frac{p_0}{p_m}\right)^{1-\beta}\left(\frac{R_t}{R_{t0}}\right)^{-\beta}, \\ &\dot R_{ex} = v_m\left(\frac{p_0 A_t}{p_m A_{ex}}\right)^{1-\beta}\left(\frac{R_{ex}}{R_{ex0}}\right)^{-\beta}\frac{\left(T_{ex} - T_{abl}\right)}{\left(T_t - T_{abl}\right)}, \\ &\dot R_h = \frac{Q_c + Q_R + Q_b}{\left[q_{met} + C_{met}\left(T_{mel} - T_{m0}\right)\right]\rho_{met}}, \end{aligned} \tag{17}$$

where the following dimensionless variables are used

$$p \to \frac{p_0}{p_m},\ \rho \to \frac{\rho_0}{\rho_m},\ t \to \frac{t r_b(p_m)}{L_0},\ R_t \to \frac{R_t}{L_0},\ A_b \to \frac{A_b}{L_0^2},\ V \to \frac{V}{L_0^3},\ R_{t,h} \to \frac{R_{t,h}}{L_0},\ R \to \frac{R}{L_0},\ A_{et} \to \frac{A_{et}}{L_0^2}. \tag{18}$$

Here subscript m refers to maximum reference values of the pressure and density and L_0 is characteristic length of the motor. We note that two first equations in (17) correspond to the "filling volume" approximation in (Salita, 1989 & 2001). The important difference is that we have introduced noise terms and the exact dependence of the burning surface on the burn distance in the form of the design curve relation in the fourth equation in (17). We have also established an explicit connection with the set of partial differential equations (1) that helps to keep in order various approximations of the Eqs. (1), which are frequently used in practice and in our research.

The equations above have to be completed by the equations for the main thrust F and lateral (side) thrust F_h induced by the gas flow through the hole in the form

$$F = \Gamma^{-1}\sqrt{\gamma\rho_0 p_0}\,A_t u_{ex} + (p_{ex} - p_a)A_{ex}, \quad F_h = \Gamma^{-1}\sqrt{\gamma\rho_0 p_0}\,A_{t,h} u_{h,ex} + (p_{ex,h} - p_a)A_{h,ex} \qquad (19)$$

where p_a is ambient pressure, u_{ex} and $u_{h,ex}$ are gas velocities at the nozzle outlet and hole outlets respectively, and p_{ex} and $p_{h,ex}$ are the exit pressure at the nozzle outlet and hole outlets respectively.

3.2 Axial distributions of the flow variables in a sub-scale motor

It follows from the analysis that $M_0^2 = v^2/c_0^2 \ll 1$ is small everywhere in the combustion chamber. Furthermore, the equilibration of the gas flow variables in the chamber occurs on the time scale ($t = L/c$) of the order of milliseconds. As a result, the distribution of the flow parameters follows adiabatically the changes in the rocket geometry induced by the burning of the propellant surface, nozzle ablation and metal melting in the hole through the case. Under these conditions it becomes possible to find stationary solutions of the Eqs. (1) analytically in the combustion chamber. Taking into account boundary conditions at the stagnation point and assuming that the spatial variation of the port area $A_p(x)$ is small and can be neglected together with axial component of the flow at the propellant surface $u_S(x)$, we obtain the following equations for the spatial variation of the flow parameters (Osipov et al., March 2007)

$$\left(S\rho u\right)\Big|_0^x = \int_0^x \rho_p r_b l dx, \quad \rho u^2 + p = p_0, \quad \left(S\rho h_t u\right)\Big|_0^x = H\int_0^x \rho_p r_b l dx. \qquad (20)$$

$$\rho = \rho_0\left(1+\frac{\gamma+1}{2}\frac{u^2}{c_0^2}\right)^{-1}, \; p = p_0\left(1+\frac{\gamma+1}{2}\frac{u^2}{c_0^2}\right)^{-1}\left(1-\frac{\gamma-1}{2}\frac{u^2}{c_0^2}\right)^{-1}, \; v = \frac{u_L x}{L}\left(1+\frac{3(\gamma+1)-2n\gamma)}{6c_0^2}u_L^2\frac{x^2}{L^2}\right). \qquad (21)$$

and in the nozzle area

$$p = p_0\left(1-\frac{(\gamma-1)}{2}M_0^2\right)^{\frac{\gamma}{\gamma-1}}, \quad \rho = \rho_0\left(1-\frac{(\gamma-1)}{2}M_0^2\right)^{\frac{1}{\gamma-1}}, \quad T = T_0\left(1-\frac{(\gamma-1)}{2}M_0^2\right), \qquad (22)$$

where M_0 is given by the solution of the nozzle equation

$$M_0\left(1-\frac{(\gamma-1)}{2}M_0^2\right)^{\frac{1}{\gamma-1}} = \frac{A_t}{\Gamma A}.$$

3.3 Verification and validation (V&V) of the "filing volume" model

To verify the model we have performed high-fidelity simulations using code by C. Kiris (Smelyanskiy et al., 2006) and FLUENT model (Osipov et al., 2007; Luchinsky et al., 2008). To solve the above system of equations numerically we employ a dual time-stepping scheme with second order backward differences in physical time and implicit Euler in psuedo-time, standard upwind biased finite differences with flux limiters for the spatial derivative and the source terms are evaluated point-wise implicit. For these simulations the following geometrical parameters were used: initial radius of the grain R_0 = 0.74 m, R_t = 0.63 m, L = 41.25m; ρ = 1800 kg·m^{-3}, H = 2.9x106 J·kg^{-1}, r_c = 0.01 m·sec^{-1}, p_c = 7.0x10^6 Pa. The results of integration for a particular case of the neutral thrust curve are shown in the Fig. 1(b). The fault (the nozzle throat radius is reduced by 20%) occurs at time t_f = 15 sec. The comparison of the results of the simulations of the model (1) with the solution of the LDM (17) is shown in the Fig. 3(a). It can be seen from the figure that the LDM reproduces quite accurately the dynamics of the internal density in the nominal and off-nominal regimes. Similar agreement was obtained for the dynamics of the head pressure and temperature.

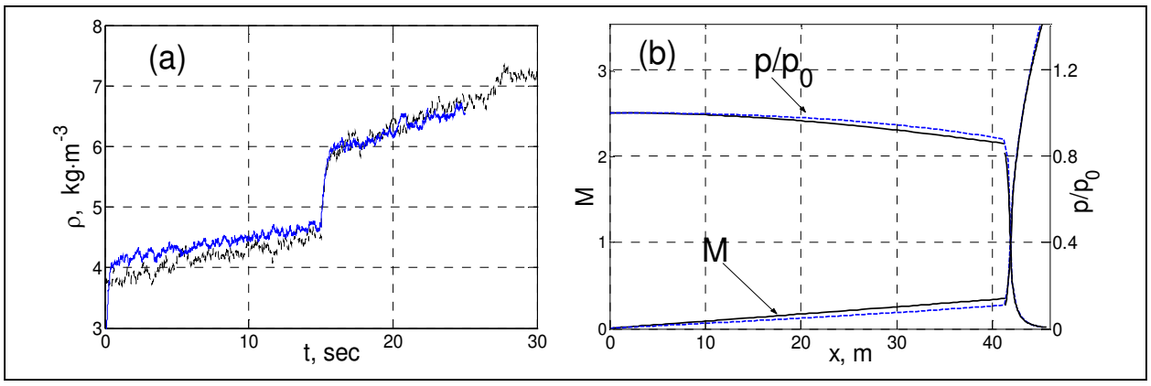

Fig. 3. (a) Comparison between the results of integration of the stochastic partial differential equations Eqs. (1), (2)(solid blue lines) and stochastic ordinary differential equations Eqs. (17)(dotted black lines) for the time evolution of the head density. (b) Comparison between the numerical (dashed blue lines) and analytical (solid lines) solutions for the gas velocity and pressure.

The comparison of the analytical solution (21), (22) for axial distribution of the pressure and velocity with the results of numerical simulation of the high-fidelity model is shown in the Fig. 3(b). It can be seen from the figure that the axial variation of the gas flow parameters is small and agrees well with the results of numerical integration. Therefore, the dynamics of the SRMs operation with small variation of the port area along the rocket axis can be well characterized by the LDM (17), obtained by integration of Eqs. (1), (2) over the length of the combustion camera.

This conclusion is also supported by the 2D high-fidelity simulations using FLUENT. To simulate time evolution of the propellant regression, nozzle ablation, and the hole burning through we have introduced the following deforming zones (see Fig. 4): (i) hole in the forward closure; (ii) nozzle ablation; and (iii) variation of the burning area as a function of time. In simulations we have used a density based, unsteady, implicit solver. The mesh was initialized to the stagnation values of the pressure, temperature, and velocity in the combustion chamber and to the ambient values of these variables in the two ambient

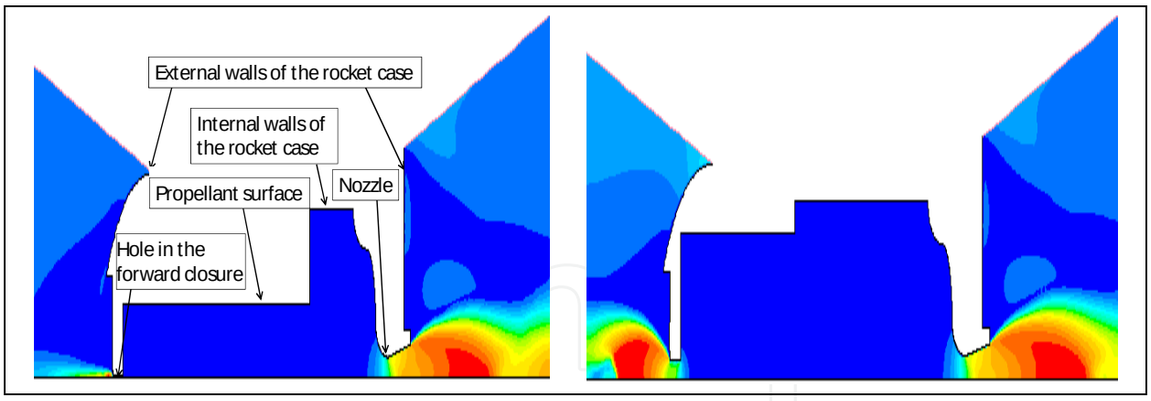

Fig. 4. 2D velocity distribution with axial symmetry obtained using FLUENT simulations after 0.14 sec (left) and t = 5.64 (right). The geometry of the model surfaces is shown in the figure. The propellant surface wall, hole wall, and the nozzle wall are deforming according to the equations (2), note the changes in the geometry of the rocket walls and the corresponding changes in the velocity distribution.

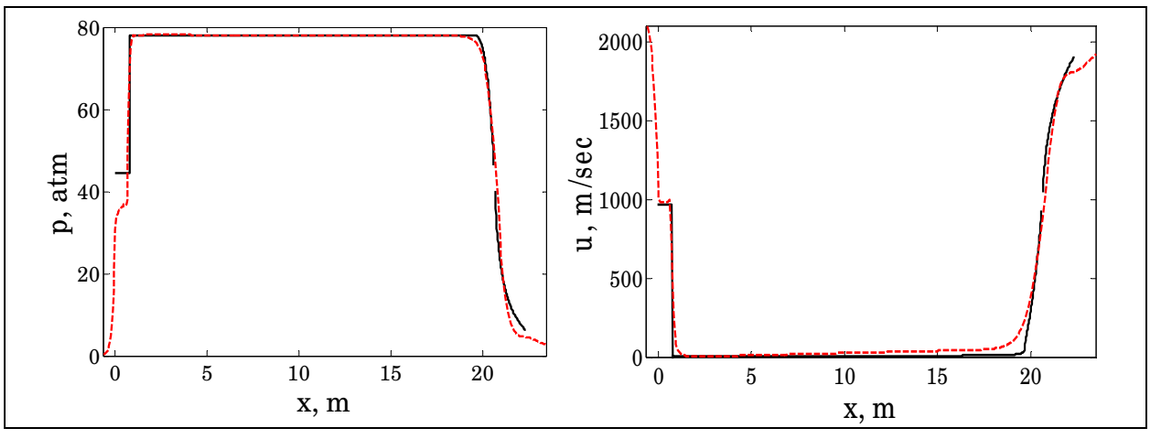

Fig. 5. Axial velocity (left) and pressure (right) profiles generated by the FLUENT model for t=0.05 sec (red dashed line) as compared to the analytical solutions (black solid lines) given by the (21), (22).

regions on the right and left of the chamber. The results of the comparison of the analytical distributions (21)-(22) with the axial velocity and pressure distributions obtained using FLUENT simulations are shown in the Fig. 5. It can be seen from the figure that the model (17), (21)-(22) provides a very good approximation to the results of FLUENT simulations.
Note that the difference in the time scales for dynamics of burn distance, metal erosion, and nozzle ablation as compared to the characteristic relaxation time of the distributions to their quasi-stationary values t_{rel} allows us to integrate equations (1), (2) in quasi-stationary approximation as will be explained in details in Sec. 5. As a result we obtain the analytical solution for the quasi-stationary dynamics of the axial distributions of the gas parameters in the combustion chamber and in the nozzle area. The comparison of this analytical solution with the results of FLUENT simulations also demonstrates agreement between the theory and numerical solution of the high-fidelity model. The accuracy of the low-dimensional model (17) was further validated using results of a ground firing test for a subscale motor as will be described in details elsewhere.

4. Bayesian inferential framework for internal SRMs ballistics

We are now in a position to introduce a novel Bayesian inferential framework for the fault detection and prognostics in SRMs. Note that the effect of the case breach fault and nozzle blocking on the dynamics of the internal gas flow in SRMs is reduced to the effective modification of the nozzle throat area $A_{et}(t)$ as explained above. In a similar manner the effects of bore choking and propellant crack can be taken into account by introducing an effective burning area and by coupling the analysis of the pressure time-traces with the analysis of the nozzle and side thrust. The accuracy of the calculations of the internal SRM ballistics in sub-scale motors in nominal and off-nominal regimes based on the LDM (17) allows us to use it to verify the FD&P in numerical simulations.

4.1 Bayesian framework

The mathematical details of the general Bayesian framework are given in (Luchinsky et al., 2005). Here we briefly introduce earlier results in the context of fault detection in SRMs including abrupt changes of the model parameters. The dynamics of the LDM (17) can be in general presented as an Euler approximation of the set of ODEs on a discrete time lattice $\{t_k=hk;\ k=0,1,...,K\}$ with time constant h

$$x_{k+1} = x_k + hf(x_k^* \mid c) + \hat{\sigma}\sqrt{h}z_k, \tag{23}$$

where $z_k = \frac{1}{\sqrt{h}}\int_{t_k}^{t_k+h}\xi(t)dt$, $x_k^* = \frac{x_k + x_{k+1}}{2}$, $\boldsymbol{x_k} = \{p, \rho, R, V, r_h, r_t, r_i\}$ is L-dimensional state of the system (17), σ is a diagonal noise matrix with two first non-zero elements a_1 and a_2, $\boldsymbol{f}$ is a vector field representing the rhs of this system, and c are parameters of the model. Given a Gaussian prior distribution for the unknown model parameters, we can apply our theory of Bayesian inference of dynamical systems (Luchinsky et al., 2005) to obtain

$$D_{ij} = \frac{h}{K}\sum_{k=0}^{K-1}(\dot{x}_k - f(x_k;c))_i(\dot{x}_k - f(x_k;c))_j \tag{24}$$

$$c'_l = \left(A\right)^{-1}_{ml} w_m, \tag{25}$$

where elements A_{ml} and w_m are defined by the following equations

$$w_m = h\sum_{k=0}^{K-1}\left[\sum_{n,n'=1}^{L} U'_{mn}(t_k)D^{-1}_{nn'}\dot{x}_{n'}(t_k) - \frac{v_m}{2}\right] \tag{26}$$

$$A_{ml} = h\sum_{k=0}^{K-1}\left[\sum_{n,n'=1}^{L} U'_{mn}(t_k)D^{-1}_{nn'}U_{n'l}(t_k)\right]. \tag{27}$$

Here the vector field is parameterized in the form $f(x;c)=\hat{U}(x)c$, where $\hat{U}(x)$ is a block-matrix with elements U_{mn} build of N blocks of the form $\hat{I}\phi_n(x(t_k))$, $\hat{I}$ is LxL unit matrix, and

$$v_m(\mathbf{x}) = \sum_{n=1}^{N} \frac{\partial U_{nm}(\mathbf{x})}{\partial x_n}.$$

To verify the performance of this algorithm for the diagnostics of the case breach fault we first assume the nominal regime of the SRM operation and check the accuracy and the time resolution with which parameters of the internal ballistics can be learned from the pressure signal only. To do so we notice that equations for the nozzle throat radius r_t, burn distance R, and combustion chamber volume can be integrated analytically for a measured time-traces of pressure and substituted into the equations for pressure dynamics. By noticing further that for small noise-intensities the ratio of dimensionless pressure and density $p/\rho \approx 1$ obtain the following equation for the pressure dynamics

$$\dot{p} = -\frac{c_0 \gamma \Gamma A_{et}}{V r_b} p + \frac{A_b}{V}\left(\gamma \rho_p - p\right) p^n + \sqrt{D}\xi_2(t), \tag{28}$$

where $A_t(t)$, $A_b(t)$, and $V(t)$ are known functions of time given by the following equations

$$\begin{aligned} &R(t) = \int_0^t p^n(t')dt', \quad A_b(t) = f\left(R(t)\right), \quad V(t) = V_0 + \int_0^{R(t)} A_b(R)dR, \\ &A_t(t) = \pi r_t^2(t), \quad R_t(t) = \left[R_{t0}^{1+\beta} + v_m(1+\beta)\int_0^t p^{1-\beta}(t')dt' \right]^{\frac{1}{1+\beta}} \end{aligned} \tag{29}$$

The parameters $c_0\gamma\Gamma/r_b$, $\gamma\rho_p$, and D can now be inferred in the nominal regime by applying Eqs. (23)-(27) to the analysis of equation (28). An example of the inference results is shown in the Table 1.

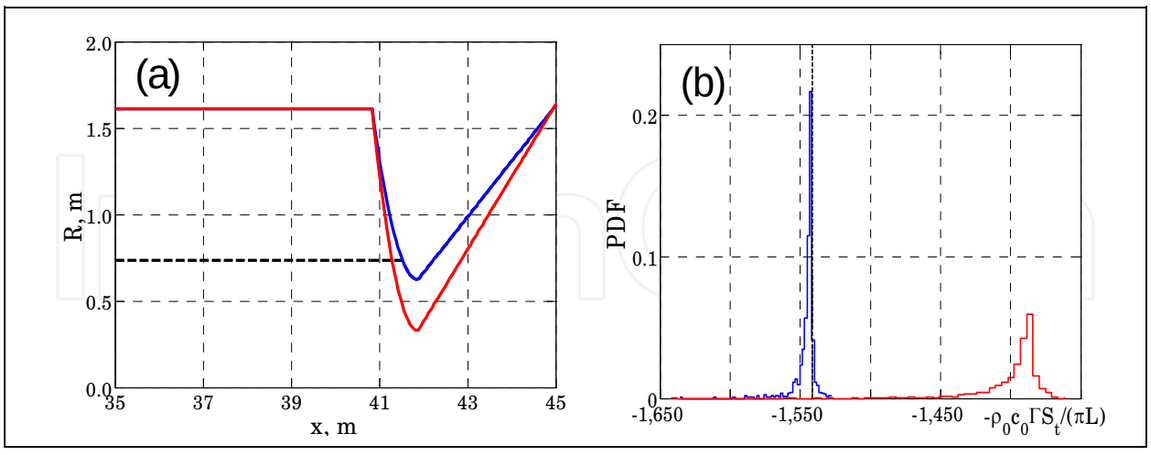

Fig. 6. (a) An example of the geometry of the simulations of the nozzle failure model using Eqs. (1), (2). The geometry of the case before and after the fault is shown by the solid blue and red lines respectively. (b) estimation of the value of the parameter $-c_0GA_t/(pL)$ before (left curve) and after (right curve) the fault. The dashed line shows the actual value of the parameter. The solid lines show the PDF of the parameter estimation with T=0.1 sec, Δt=0.001 sec, N=500 (see the caption for the Table 1).

Parameters	Actual	Inferred	Relative error
$\gamma\rho_p$	248.2	244.7	1.4%
$-c_0\Gamma/r_b$	-61260	-61347	1.38%
D	2.5×10^{-4}	2.44×10^{-4}	2.4%

Table 1. The results of the parameter estimation of the model (28), (29) in the nominal regime. The total time of the measurements in this test was T=1 sec, the sampling rate was 1 kHz, and the number of measured points was N=1000.

We conclude that the parameters of the nominal regime can be learned with good accuracy during the first few second of the flight. This result allows one to apply Bayesian algorithm for fault detection and diagnostics in SRMs.

We now provide numerical example explaining in more details how this technique can be used for in-flight FD&P in SRMs. We will be interested to verify if the Bayesian framework can provide additional information ahead of the "alarm" time about the most likely course of the pressure dynamics to reduce the probability of the "misses" and "false alarms". To model the "miss" situation a case will be considered when small pressure deviation from the nominal value persists for a few second prior to the crossing the "alarm" level and the time window between the "alarm" and "catastrophe" becomes too short. This situation is illustrated in the Fig. 7(a), where measured pressure signal (black solid line) crosses the alarm level (dashed line) initiating the alarm at approximately $t_A \approx 15$ sec. The overpressure fault occurs at $t_F \approx 17$ sec and the time window between the alarm and a "catastrophic" event becomes too short, which can be considered as a model of "miss" situation. To model the "false alarm" situation a case will be considered in which the pressure crosses the "alarm" level, but then returns to its nominal value (see Fig. 7(b)). In all the simulations presented here the overpressure fault was modeled as a reduction of the nozzle throat area. Note, however, that the results discussed below can be extended to encompass other faults, including e.g. the propellant cracking, bore choking, and case breach as will be discussed below.

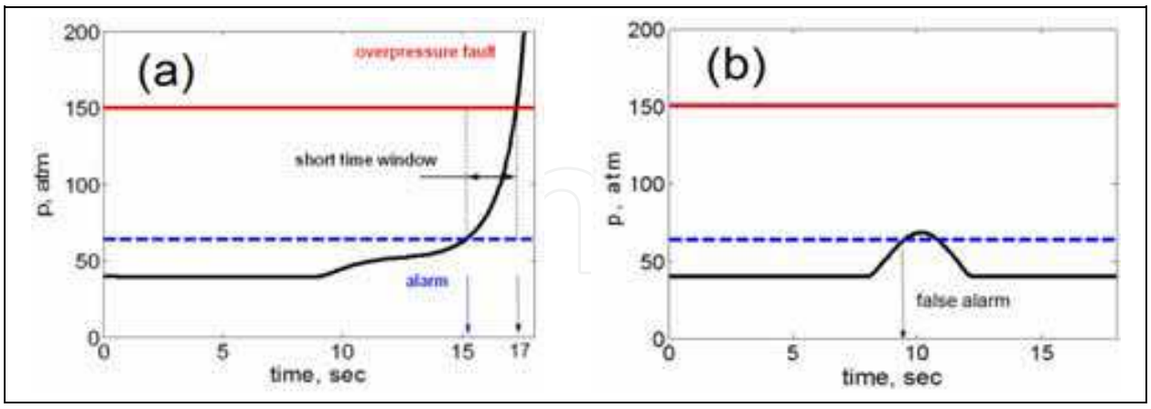

Fig. 7. (a) Example of possible time variation of the pressure fault (black line) representing a possible "miss" situation. The blue dashed and red solid lines indicate the "alarm" and the "catastrophe" levels respectively. Note that the time window between the "alarm" and the "catastrophe" is too short. (b) Example of possible time variations of the fault pressure representing a possible "false alarm" situation. The blue dashed and red solid lines are the same as in (a).

4.2 Modeling "misses" for the nozzle failure and neutral thrust curve

To model the "misses" we assume that the time evolution of the nozzle fault is highly nonlinear and can be described by a polynomial function

$$A_{et} = A_{t0} - \Delta A\left(\alpha\tau + \beta\tau^2 + \delta\tau^3\right) \tag{30}$$

corresponding e.g. to the slow degradation followed by the fast destruction of the nozzle walls as shown in the Fig. 7(a), where τ is the time elapsed from the fault initialization. In this case the time window between the "alarm" and the overpressure fault becomes too short and effectively the FD&P system "misses" the event. The thrust curve is chosen to be neutral. Our goal is to demonstrate that application of the Bayesian framework for the SRM FD&P allows one to extend substantially the time window between the "alarm" and the overpressure fault thereby reducing the probability of "misses". To this end we extend the model described by Eqs. (17) by including nonlinear terms from Eq.(30). The corresponding vector field of the Eq. (28) can be written as $f(x;c)=\hat{C}\phi$ with the set of the base functions given by Eq. (31) and the set of the model parameters is given in Eq.(32), where $a=(c_0 I)/(\pi L r_{b0} R^*)$.

$$\vec{\phi} = \left\{ p^n, \frac{p^n}{R}, \frac{p^{n+1}}{R}, \frac{p^n\rho}{R}, \sqrt{\frac{p}{\rho}}\frac{p}{R}, \sqrt{\frac{p}{\rho}}\frac{p\tau}{R}, \sqrt{\frac{p}{\rho}}\frac{p\tau^2}{R}, \sqrt{\frac{p}{\rho}}\frac{p\tau^3}{R}, \ldots \right.$$
$$\left. \sqrt{\frac{p}{\rho}}\frac{\rho}{R}, \sqrt{\frac{p}{\rho}}\frac{\rho\tau}{R}, \sqrt{\frac{p}{\rho}}\frac{\rho\tau^2}{R}, \sqrt{\frac{p}{\rho}}\frac{\rho\tau^3}{R} \right\} \tag{31}$$

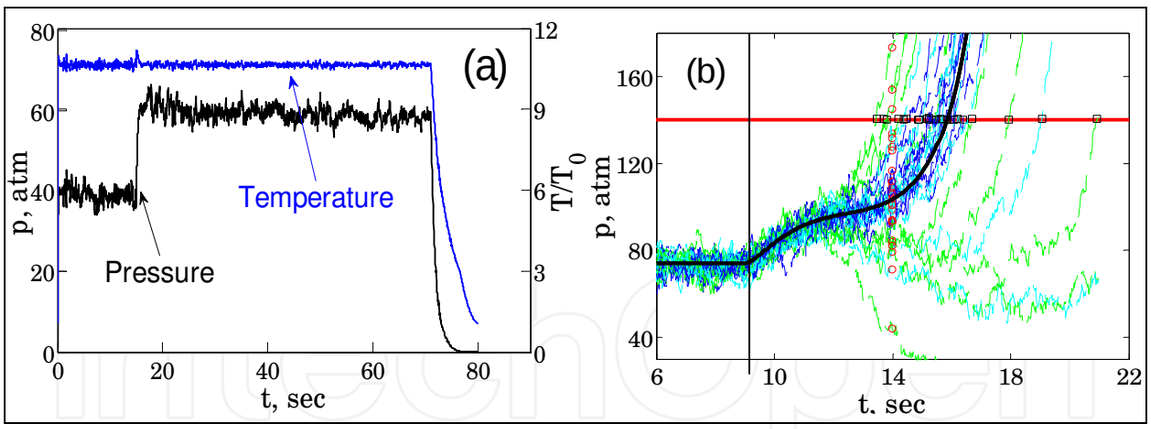

Fig. 8.(a) An example of the time-traces of temperature (blue line) and the pressure (black line) of the SRM operation with neutral thrust curve. Fault corresponding to abrupt changes of the nozzle throat area (cf Fig. 6(a)) occurs at t=17 sec. (b) Nonlinear time evolution of the pressure build up after the nozzle blocking fault is shown by the back solid line. Predicted dynamics of the pressure is shown by the jiggling lines. The results of the predictions build 1sec, 1.5sec, and 2.1 sec after the fault are shown by green, cyan, and blue lines correspondingly. The values of the pressure at t=14 sec, which are used to build the PDF of the pressure, are shown by red circles. The time moments of the predicted overpressure faults used to build the PDF of the case burst times as shown by the black squares on the red margin line. Fault occurs at t=9 sec.

$$\hat{C} = \begin{bmatrix} 0 & 2\gamma\rho_p & -2 & 0 & -a\gamma & -a\gamma\alpha & -a\gamma\beta & -a\gamma\delta & 0 & 0 & 0 & 0 \\ 0 & 2\rho_p & 0 & -2 & 0 & 0 & 0 & 0 & -a & -a\alpha & -a\beta & -a\delta \\ 1 & 0 & 0 & 0 & 0 & 0 & 0 & 0 & 0 & 0 & 0 & 0 \end{bmatrix} \quad (32)$$

Parameters of the system are monitored in real time. Once small deviations from the nominal values of the parameters is detected at time t_d the algorithm is continuously updating the inferred values of parameters estimated on increasing intervals Δt of time elapsed from t_d . These values are used to generate a set of trajectories predicting pressure dynamics. Example of such sets of trajectories calculated for three different time intervals Δt =1sec, 1.5 sec, and 2.1 sec are shown in the Fig. 8(b) by green, cyan, and blue lines respectively. These trajectories are used to predict the PDFs of the head pressure for any instant ahead of time. An example of such PDF for the pressure distribution at time at t=14 sec is shown in the Fig. 9(a). The method used to calculate PDF for the pressure distributions is illustrated in the Fig. 8(b). The same trajectories are used to predict the PDFs of the time moment of the overpressure fault as illustrated in the Fig. 8(b) and Fig. 9(b). It can be seen from the figures that the distribution of the predicted time of the overpressure fault converges to the correct value 2.1 sec after the fault thereby extending the time window between the "alarm" and the fault to 6 sec which is almost three folds of the time window obtained using standard technique.

Therefore, we conclude that the Bayesian framework provides valuable information about the system dynamics and can be used to reduce the probability of the "misses" in the SRM FD&P system. A similar analysis shows (Luchinsky et al., 2007) that the general Bayesian framework introduced above can be applied to reduce the number of "false alarms".

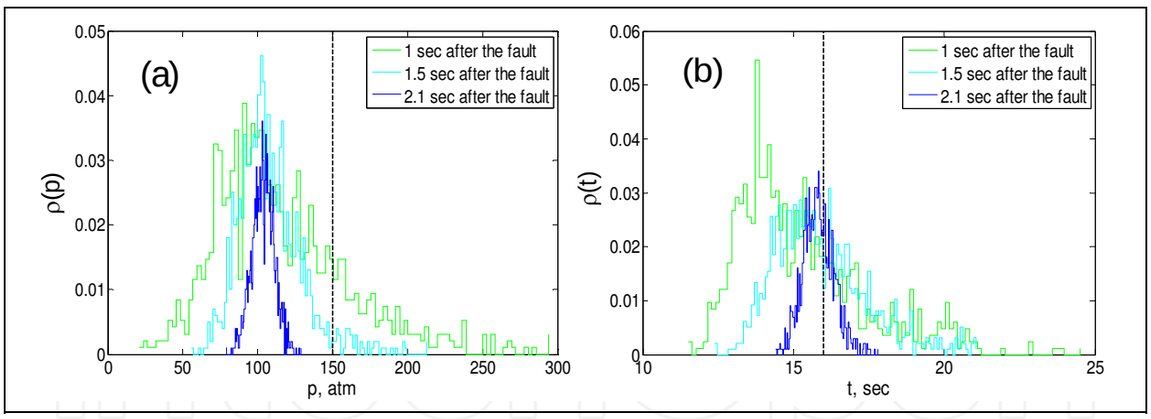

Fig. 9. (a) The PDF of the predicted values of pressure at t=14 sec build 1 sec (green line), 1.5 sec (cyan line), and 2.1 sec (blue lines) after the fault. The dashed vertical line shows the dangerous level of the pressure. (b) The PDF of the predicted times of the overpressure fault build 1sec (green line), 1.5 sec (cyan line), and 2.1 sec (blue lines) after the fault. The dashed vertical line shows the actual time when the overpressure fault is going to happen.

4.3 Self-consistent iterative algorithm of the case breach prognostics

In the previous section we have shown that in-flight FD&P for SRMs can be developed within Bayesian inferential framework. The introduced technique can be very useful in a wide range of contexts including in particular active control of combustion instabilities in

liquid motors (Hathout et al, 2002). In practice, however, it is often desirable (see also the following section) to further simplify the algorithm by avoiding stochastic integration. The simplification can be achieved by neglecting noise in the pressure time-traces and by considering fault dynamics in a regime of quasi-steady burning.

To illustrate the procedure of building up iterative FD&P algorithms that avoids stochastic integration let us consider the following example problem. A hole through the metal case and insulator occurs suddenly at the initial time of the fault t_0. The goal is to infer and predict the dynamics of the growth of the holes in the insulator layer and in the metal case, as well as the fault-induced side thrust, and changes to the SRM thrust in the off-nominal regime. In this example the model for the fault dynamics is assumed to be known. This is a reasonable assumption for the case breach faults with simple geometries. For this case the equations can be integrated analytically in quasi-steady regime and the prognostics algorithm can be implemented in the most efficient way using a self-consistent iterative procedure, which is developed below. As an input, we use time-traces of the stagnation pressure in the nominal regime and nominal values of the SRM parameters. In particular, it is assumed that the ablation parameters for the nozzle and insulator materials and the melting parameters for the metal case are known. It is further assumed that the hole radius in the metal case is always larger than the hole radius in the insulator (i.e. the velocity of the ablation of the insulator material is smaller than the velocity of the melting front), accordingly the fault dynamics is determined by the ablation of the insulator. This situation can be used to model damage in the metal case induced by an external object.

To solve this problem we introduce a prognostics algorithm of the fault dynamics based on a self-consistent iterative algorithm that avoids numerical solution of the LDM. We notice that with the limit of steady burning, the equations in (17) can be integrated analytically. Because the hole throat is determined by the radius of the hole in the insulator, we can omit the equation for the hole radius in the metal case. The resulting set of equations has the form

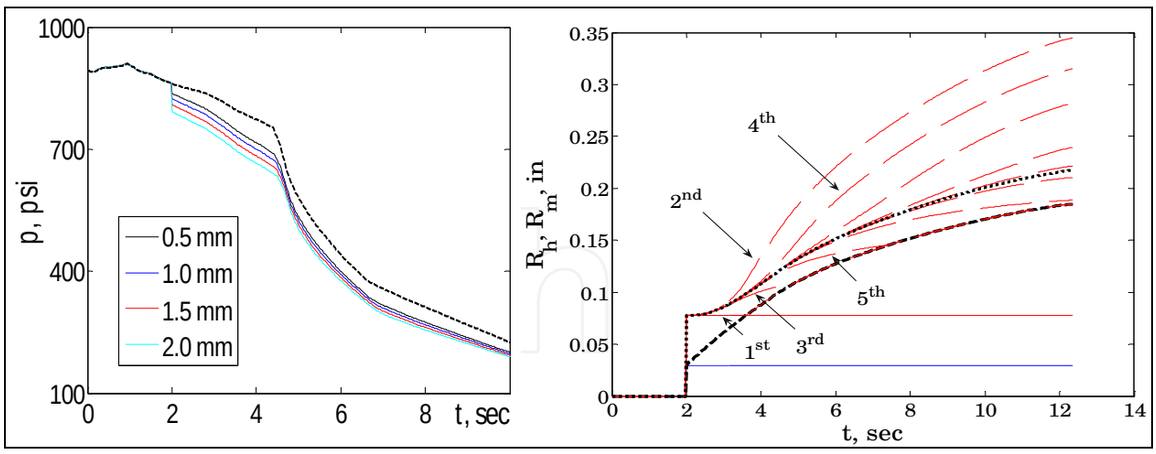

Fig. 10. (left) Results of the calculations using iterative algorithm A1. Absolute values of pressure for four different initial values of the hole in the case: 0.5, 1.0, 1.5 and 2.0 mm are shown by the black, blue, red, and cyan solid lines respectively. The nominal pressure is shown by the dashed black line. (right) Iterations of the effective hole radius in the metal case. Red solid line shows 0th approximation. Five first approximations shown by red dashed lines are indicated by arrows. Final radius of the hole in the metal case is shown by black dotted line. 0th approximation for the hole in the insulator is shown by dashed blue line. Final radius of the hole in the insulator is shown by the black dashed line.

$$\begin{cases} p(t) = p_N(t)\left[\dfrac{A_{bef}(t)A_t(t)}{A_b A_{et}(t)}\right]^{\frac{1}{1-n}}, \\ R = a\int_0^t p^n(\tau)d\tau, \\ R_t^{1+\beta_t}(t) = R_{t0}^{1+\beta} + (1+\beta)v_{n0}\int_{t_0}^t p^{1-\beta}(\tau)d\tau, \\ R_h^{1+\beta_i}(t) = R_{h0}^{1+\beta_i} + (1+\beta)v_{h0}\int_{t_0}^t p^{1-\beta}(\tau)d\tau. \end{cases} \quad (33)$$

Here $A_{et}(t) = A_t(t) + \Delta A_t(t) + A_h(t)$ is an effective nozzle throat area where the 1st term corresponds to the nominal regime, the 2nd term corresponds to the deviation of the nozzle throat area from the nominal regime due to the fault, and the 3rd term corresponds to the area of the hole in the rocket case. Similarly, we define the effective burning area $A_{bef}(t) = A_b(t) + \Delta A_b(t)$ as a sum of the burning area in the nominal regime and a term that describes the deviation of the burning area from the nominal regime due to the fault. Using Eqs (33) the following iterative algorithm **A1** can be introduced:

1. Set initial values of the corrections to the nozzle and burning area to zero $\Delta A_t(t) = 0$ and $\Delta A_b(t)=0$. Set values of the areas of the holes in the metal and in the insulator to constant initial values $A_m(t) = \pi \cdot R_{m0}^2$ and $A_h(t) = \pi \cdot R_{h0}^2$.
2. Update time-trace of the pressure using 1st eq. in (33)
3. Update burn web distance R, radius of the hole in the insulator R_h, and nozzle throat radius R_t using last three Eqs. In (33).
4. Repeat from the step (2) until convergence is reached.

The results of the application of this self-consistent algorithm to the prognostics of the case breach fault parameters are shown in Fig. 10(left). Once quasi-steady pressure and the dynamics of the hole growth in the insulator are predicted in the off-nominal regime one can determine the dynamics of the hole growth in the metal case and the dynamics of the fault-induced side thrust. To do so, we use the following self-consistent iterative algorithm **A2** for $t>t_0$ that takes into account the assumption that the velocity of the melting front is larger than the velocity of ablation in the insulator.

1. Set 0th approximation $R^{(0)}{}_{h0}(t)$ for the hole radius in the metal to r_{h0}.
2. Construct 1st approximation

$$R_m^{(1)}(t) = \begin{cases} R_m^{(0)}(t), & \text{if } R_m^{(0)}(t) > R_h(t) \\ R_h(t), & \text{if } R_m^{(0)}(t) \le R_h(t) \end{cases}$$

3. Solve Mach equation (use a maximum root)

$$M_0(t) = \begin{cases} M_0\left(1 - \dfrac{\gamma-1}{2}M_0^2\right)^{\frac{1}{\gamma-1}} = \dfrac{A_h}{\Gamma A_m}, & \text{if } R_m^{(0)}(t) > R_h(t) \\ \dfrac{c_t}{c_0} = \sqrt{\dfrac{2}{\gamma+1}}, & \text{if } R_m^{(0)}(t) \le R_h(t) \end{cases}$$

4. Find the effective radius of the hole in the metal case

$$R_m^{1+\beta} = R_{m0}^{1+\beta} + v_{m0}\int_{t_0}^{t}\left(\frac{(\rho v)_m(\tau)}{(\rho v)_*^{\max}}\right)^{1-\beta}\left(\frac{T_m(\tau)-T_{mel}}{T_t-T_{mel}}\right)d\tau$$

5. Use Eqs (21)-(22) to find velocity $u_m(t)=M_{0m}(t)\cdot c_0$, mass flow $(\rho u)_m(t)$, temperature $T_m(t)$, and pressure $p_m(t)$ in the metal hole;
6. Repeat from the step (2) until convergence is reached.
7. Calculate fault-induced side thrust $F_h = \left[(\rho u)_m u_{m,ex} + (p_{m,ex} - p_a)\right] S_m$.

A similar algorithm is used to find the ablation of the nozzle and SRM thrust in the off-nominal regime in the case breach fault. The results of these calculations are shown in Fig. 10(right) and Fig. 11. We note that the fault diagnostics is achieved using the same iterative algorithm with the only exception being that the time-trace for pressure in the off-nominal regime is given by the measurements. Accordingly the first equation in the set (33) and the 2nd step in the iterative algorithm **A1** are not needed. Also note that an important feature of the algorithms introduced above is the assumption that the design curve $A_b = f(R)$ representing the relation between the burning area A_b and burn web distance R is known and remains invariant characteristics of the SRM in the off-nominal regime of the case breach fault.

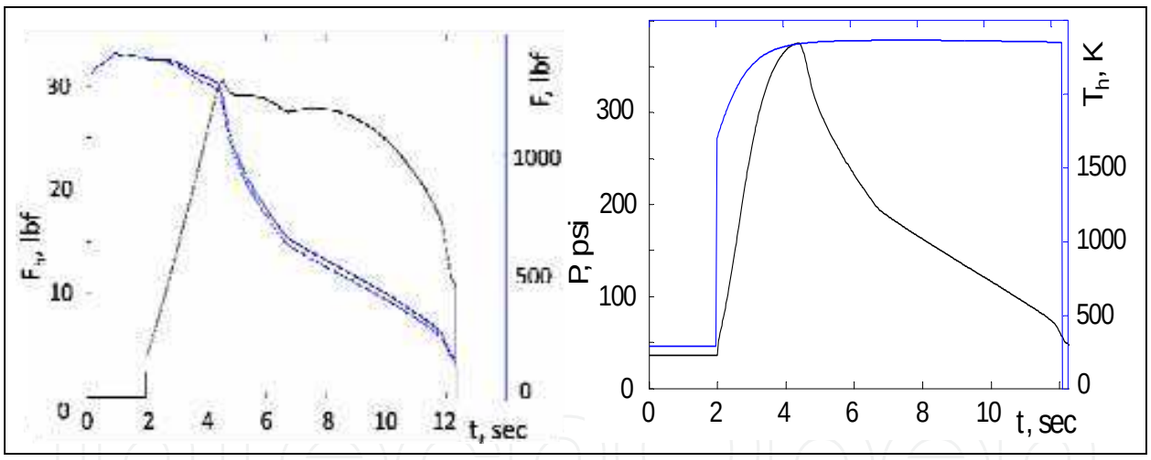

Fig. 11. (left) Fault-induced thrust (black solid line) is shown in comparison with nominal SRM thrust (blue solid line) and off-nominal SRM thrust (dashed blue line). Initial radius of the hole in the insulator is 0.75mm. (right) Pressure (black line) and temperature (blue line) in the metal hole through the case determined by the iteration algorithm A2.

The deep physical meaning of the iterative procedure introduced above rests upon the idea that the ablation of the hole walls and the case breach fault develop in a self-consistent manner. Indeed, the increase of the cross section leak, due to insulator ablation under the action of the hot gas flow, leads to decreased pressure and hence a decreased burning rate. This, in turn, decreases the hot gas flow through the hole and the ablation rate. In this way a quasi-stationary regime of burning and ablation is developed. The parameters of burning in this regime can be found in a self-consistent way using an iterative algorithm, without integration of the full system of differential equations of motion.

If the fault dynamics is determined by hole growth rate in the metal case the algorithm above is still applicable and can be substantially simplified, because the ablation in the isolator can be neglected and sonic condition holds in the hole throat. The resulting algorithm is algorithm **A1** extended using one equation from step 7 of algorithm **A2**. We now consider how the FD&P system can be extended to a large segmented motor. In what follows the fault dynamics is determined by hole growth rate in the metal case, which is the most plausible situation in practice.

5. FD&P for large segmented SRMs

To extend the FD&P algorithm to a large segmented motor we will first simplify the model of its internal ballistic in the nominal and off-nominal regimes introduced in Sec. 2. Combining the equations of gas dynamics with the dynamics of propellant regression, nozzle ablation, and case breach fault the performance model of the large segmented SRM in the presence of faults can be summarized in the set of Eqs. (34) with the conservative variables U and function $f(U)$ given by Eq. (2) and the source terms S given by Eq. (3) with neglected noise terms.

$$\begin{cases} \partial_t\left(UA_p\right)+\partial_x\left(f(U)A_p\right)=S, \\ A_p(x_i)=f_{Ai}(R(x_i)), \qquad l(x_i)=f_{li}(R(x_i)), \\ \dot{R}=ap^n+C\left(I-I_{cr}\right), \\ \dot{R}_t=v_{m,t}\left(\dfrac{p_0}{p_m}\right)^{1-\beta}\left(\dfrac{R_t}{R_{t,in}}\right)^{-\beta}, \\ \dot{R}_{ex}=v_{m,ex}\left(\dfrac{p_0A_t}{p_mA_{ex,in}}\right)^{1-\beta}\left(\dfrac{R_{ex}}{R_{ex,in}}\right)^{-\beta}\dfrac{\left(T_{ex}-T_{abl}\right)}{\left(T_t-T_{abl}\right)}, \\ \dot{R}_h=\dfrac{Q_c+Q_R+Q_b}{\left[q_{met}+C_{met}\left(T_{mel}-T_{m0}\right)\right]\rho_{met}}. \end{cases} \tag{34}$$

5.1 Numerical integration of the model

We notice that (34) is a system of nearly balanced PDEs with slowly varying parameters. This is an example of PDEs with multiple time scales (Knoll et al., 2003), where the slower dynamical time scale is a result of a near balance between $\partial_x(f(U)A_p)$ and S in the first equation and slowly varying parameters in the last four equations in (34). The fast dynamics of (34) corresponds to the acoustic time scale. To see the multiple time scale character of the system (34) more clearly let us introduce dimensionless variables

$$p\to\frac{p}{p_0},\ \rho\to\frac{\rho}{\rho_0},\ \rho_p\to\frac{\rho_p}{\rho_0},\ T\to\frac{T}{T_0},\ R_N\to\frac{R_N}{L_0},\ t\to\frac{t}{t_0},\ R\to\frac{R}{L_0},\ l\to\frac{l}{L_0},\ A_p\to\frac{A_p}{L_0^2},\ u\to\frac{u}{c_0} \tag{35}$$

where $t_0 = L_0/ap_0^n \approx 10^{-2}$ sec; $p_0=p_0(t=0)$, $\rho_0=\rho_0(t=0)$ are the gas pressure and density near the rocket head at a start time point after the ignition, $M_0 = u/c_0$, $L_0 \approx 1$m are characteristics scales of time and length ($r_{p0} = ap_0^n$ is a typical burning rate). In dimensionless variables the first equation in (34) can be rewritten as follows

$$\partial_x A_p \begin{bmatrix} \rho M_0 \\ \gamma\rho M_0^2 + p \\ \rho M_0 \left(T + \frac{\gamma-1}{2} M_0^2\right) \end{bmatrix} = -\varepsilon \partial_t A_p \begin{bmatrix} \rho \\ \rho M_0 \\ \rho \left(T/\gamma + \frac{\gamma-1}{2} M_0^2\right) \end{bmatrix} + \begin{bmatrix} \varepsilon\rho_p \dot{R} l(x) + \rho_{t,h} M_{0,t} A_h \delta(x - x_0) \\ p\partial_x A_p - \gamma\lambda\rho M_0^2 l(x) \\ \varepsilon\rho_p \dot{R} l(x) + \rho_{t,h} M_{0,t} A_h \delta(x - x_0) \end{bmatrix} \tag{36}$$

Here we have introduced small parameter $\varepsilon = L_0/(t_0 c_0) < 10^{-5}$ corresponding to the ratio of the characteristic velocity of the propellant surface regression ($r_{p0} \approx 10^{-2}$ m/sec) to the speed of sound ($c_0 \approx 1006$m/sec). It is clear that in the first approximation at each given moment of time the axial distribution of the flow variables in a segmented rocket can be found in quasi-steady approximation neglecting a small last term proportional to $\varepsilon = 10^{-5}$. Note that two source terms in the 1st and 3rd Eqs. of (36) are also $\propto \varepsilon$ but these terms cannot be neglected, because they are proportional to $\rho_p \approx 10^2$.

To solve equations (36) one can neglect the first term on the right hand side $\propto \varepsilon$ and to complete resulting system of ODEs by a set of boundary conditions. The calculation of the axial distribution of the flow parameters in the quasi-steady approximation can be reduced to the integration of the system of ODEs with respect to spatial coordinate x. To this end it is convenient to write explicitly Euler approximation of Eqs. (36) in quasi-steady regime on a coarse-grained (in general non-uniform) lattice of axial coordinates $\{x_i: i=1,\ldots,N\}$

$$\begin{aligned} \rho M_0 A_p\big|_i &= \rho M_0 A_p\big|_{i+1} - \varepsilon\rho_p \dot{R} l(x) dx_i + \rho_{t,h} M_{0,th} A_h\big|_{i_h}, \\ \left(\gamma\rho M_0^2 + p\right) A_p\big|_i &= \left(\gamma\rho M_0^2 + p\right) A_p\big|_{i+1} - p\left(A_p\right)\Big|_i^{i+1} + \gamma\lambda\rho M_0^2 l(x) dx_i, \\ \rho M_0 h_T A_p\big|_i &= \rho M_0 h_T A_p\big|_{i+1} - \varepsilon\rho_p \dot{R} l(x) dx_i + h_{t,h}\rho_{t,h} M_{0,th} A_h\big|_{i_h}. \end{aligned} \tag{37}$$

where $h = \left(T + \frac{\gamma-1}{2} M_0^2\right) / H$. The dynamics of the case breach fault in this approximation is determined by the dynamics of the case breach cross-sectional area A_h. Note that the same model can be used to model other important fault modes in SRM. For example, the bore choking fault in the i^{th} ballistics element can be modeled by introducing fault induced changes to the port area A_p in this element; the crack dynamics can be modeled by introducing crack induced changes to an effective port perimeter $l(x)$ in the i^{th} ballistics element; the nozzle blocking can be modeled by introducing fault induced changes to the nozzle throat area A_t in the boundary conditions (38) below. The boundary conditions at the aft end (at the outlet of the grain) are defined by the choking (sonic) conditions at the nozzle throat. The boundary conditions at the rocket head are determined by the continuity conditions of the gas flow from the propellant surface and through the port area at the rocket head.

By adding to these two conditions the equation of state and the equation for the gas temperature in the combustion chamber as a function of the Mach number M_0 we obtain resulting boundary conditions at the rocket head (0) and aft (A) ends in dimensionless units as follows

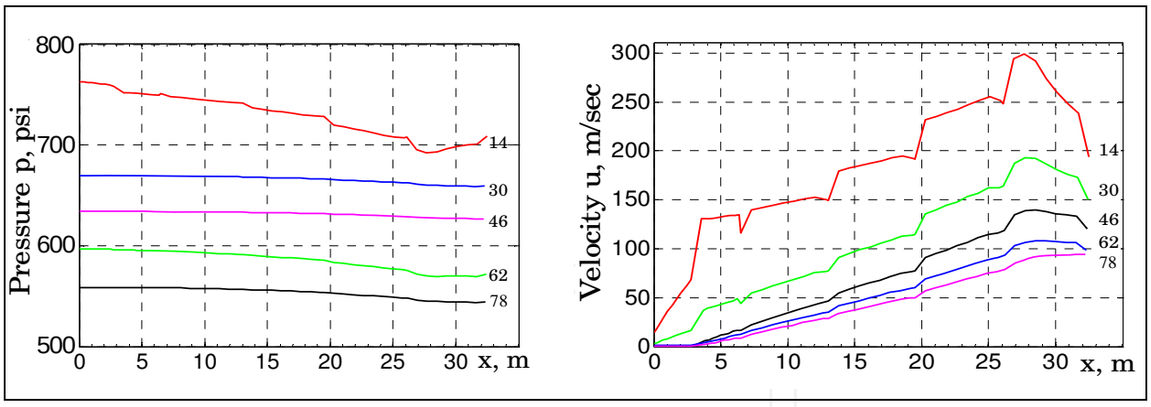

Fig. 12. Nominal regime: Results of numerical solution of Eqs. (37), (38) for axial distributions of pressure (left) and velocity (right) at different moments of time. Time after ignition: 14, 30, 46, 62, and 78 seconds. The value of x is measured from the motor head.

$$M_{0,0}=\left(\frac{\varepsilon\rho_p A_{b,0}}{A_{p,0}}\right)\left(1-\frac{\gamma-1}{2}M_{0,0}^2\right)p_0^{n-1},\ M_{0,A}\left(1-\frac{\gamma-1}{2}M_{0,A}^2\right)^{\frac{1}{\gamma-1}}=\frac{A_t}{\Gamma A_A},\ p_A=\rho_A\left(1-\frac{\gamma-1}{2}M_{0,A}^2\right). \quad (38)$$

The results of the numerical solution of the problem (37), (38) for nominal regime (A_h=0) are presented in Fig. 12. This figure shows the resulting axial distributions of the pressure and velocity for five instances of time with the time step 16 sec (the time resolution of the solution was 0.2 sec). It can be seen from Fig. 12 that there is a substantial difference between the head and aft pressure due to the effect of mass addition. The difference is most significant at the initial time when the port area is the smallest and the flow velocity has the largest values along the axis. With time the port area is increasing and the difference between head and aft pressure becomes negligible. Our analysis showed that results presented in Fig. 12 coincide with those obtained by the 3rd party using high-fidelity simulation of the internal ballistics of SRM.

5.2 Diagnostic of the fault parameters

To be able to reconstruct fault parameters first we have to introduce a parameterization of the fault. It can be seen from the model (37) that the fault dynamics is described entirely by the dynamics of the area of the hole $A_h(t)$. The actual dynamics of the fault area can be complicated due to e.g. cracks and nontrivial geometry of the joints (see e.g. (McMillin, 2006; Smelyanskiy at al., 2008)). However, analysis of the ground test results (Smelyanskiy at al., 2008) and of the challenger accident (McMillin, 2006) shows that the case breach dynamics is sufficiently smooth, primarily determined by the burning of the metal walls of the hole in the rocket case, and can be parameterized in the form:

$$A_h(t)=a_1+a_2t+a_3t^2+a_4t^3. \quad (39)$$

This parameterization has proved to be useful in the analysis of the ground firing test (Smelyanskiy at al., 2008). The parameters of the fault dynamics $\{a_1, a_2, a_3, a_4\}$ are reconstructed from the inferred time-series data $A_h(t)$ using the least square method. The hole is most likely to be localized at one of the section joints as shown schematically in Fig. 2. As a rule, only

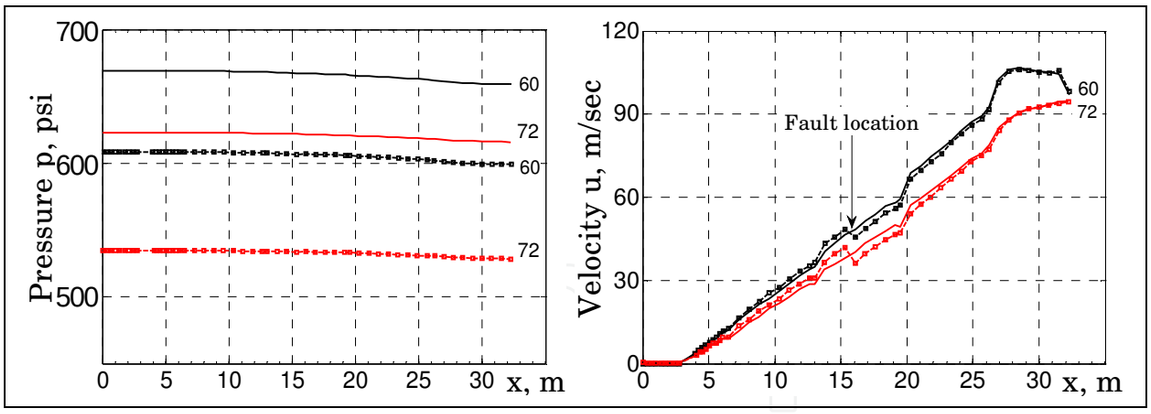

Fig. 13. (left) Comparison between spatial distribution of pressure in the nominal regime (solid lines) and off-nominal regime (squares). (right) Comparison between spatial distribution of velocity in the nominal regime (solid lines) and off-nominal regime (squares). The time instants from the top to the bottom in the figure are 60 sec and 72 sec. The time resolution of the calculations was 0.2 sec, initial radius of the hole R_{h0} = 0.1 in, burning rate of the hole wall v_m = 0.3 in/sec, initial time of the fault 20 sec, the fault is located in the middle section.

pressure sensor situated in the rocket head is available on-board. Therefore, we have to verify that the measurements of the head pressure can be used to infer pressure at an arbitrary location of the hole along the rocket axis. To do so we simulate the model of internal ballistics of the SRM (37), (38) in the off-nominal regime with the case breach area dynamics given by (39) at arbitrary location. The results of such simulations for the case breach at the middle of the SRM are shown in the Fig. 13. It can be seen from the figure that the pressure drop induced by the case breach is uniform along the rocket axis. This shift does not depend on the location of the burning-through hole in the case. In particular, this result allows one to determine the changes in the aft pressure from the measurements of the head pressure.

This finding allows us to use the following quasi-stationary solution for the nozzle stagnation pressure p_{ns}, which is hold with good accuracy for large SRMs (Salita, 1989; McMillin, 2006):

$$p_{ns} = p_c \left[\frac{\Gamma c_0 \rho_p r_c}{\gamma p_c} \left(\frac{A_{b,eff}(t)}{A_t(t) + A_h(t)} \right) \right]^{\frac{1}{1-n}}, \tag{40}$$

We notice that burning area $A_b(R(t))$ and nozzle throat area $A_t(t)$ are determined by measured gas pressure p_{ns} (see Eqs. (9) and (11)). The accuracy of the relation (40) is further improved by introducing the effective burning area $A_{b,eff}(R(t))$ in the nominal regime. Indeed, in the nominal regime $A_h(t) = 0$ while $p_{ns}(t)$ and $A_t(t)$ are well known that allows us to determine uniquely the effective burning area $A_{b,eff}(R(t))$ as a function of the burn distance $R(t)$. This functional dependence is assumed to be valid in the off-nominal regime of the case breach. Therefore, one can use data of the pressure sensor at the rocket head to estimate the deviations of the nozzle stagnation pressure p_{ns} from the nominal regime and subsequently to use equation (40) to estimate the area of the case breach fault $A_h(t)$ according to the following algorithm:

1. Use the nominal regime time-traces to determine the effective burning area by Eq. (40)

$$A_{b,eff}(t) = \left[\frac{\gamma A_t(t)}{\Gamma c_0 \rho_p a}\right] p_{ns}^{1-n}(t);$$

2. Use measured time-trace of the head pressure in the off-nominal regime $p_H(t)$ to find fault-induced pressure at the aft end using the fact that the pressure changes induced by the fault are uniform along the motor axis

$$p_A^{(fault)}(t) = p_A^{(nom)}(t) + \left(p_H^{(fault)}(t) - p_H^{(nom)}(t)\right);$$

3. Use nominal time-trace of the Mach number at the aft end to determine nozzle stagnation pressure

$$p_{ns}^{(fault)}(t) = p_A^{(fault)}(t)\left(1 - \frac{\gamma - 1}{2} M_{A,0}^2(t)\right)^{-1};$$

4. Use Eq. (40) to determine time-trace of the hole area

$$A_h(t) = \left[\frac{\Gamma c_0 \rho_p a A_{b,eff}(t)}{\gamma\left(p_{ns}^{(fault)}(t)\right)^{1-n}}\right] - A_t(t).$$

The parameters of the fault dynamics $\{a_1, a_2, a_3, a_4\}$ are reconstructed from the inferred time-series data $A_h(t)$ using the least square method. We can now use the values of the parameters $\{a_i\}$ reconstructed during the diagnostic to predict fault and internal ballistics of the SRM forward in time.

5.3 Prognostics of the fault parameters

We note that the values of the reconstructed parameters a_i of Eq. (39) depend on the diagnostics time. Therefore, the convergence of the forward predictions also depends on the diagnostic time, which is one of the key characteristics of the FD&P system. The convergence of the predicted hole area time-traces towards actual time-traces of $A_h(t)$ is illustrated in Fig. 14. In this test the hole area measurements are sampled with sampling rate 1kHz and measurement noise 0.1%. The filtering procedure is used to reduce the noise in the data. The time intervals ΔT_m used to infer fault parameters are 8 sec and 12 sec. The area of the fault is reconstructed using algorithm described in the Sec. 5.2 with the diagnostic time window 8 and 12 sec. The fault initial time is t = 40 sec. The hole radius growth rate is 0.3 in/sec. The fault parameters $\{a_i\}$ (see Eq.(39)) are inferred using e.g. noise-reduction and least-square procedures. The dynamics of the fault is predicted ahead in time up to 80 sec of the flight using inferred parameters $\{a_i\}$ and Eq.(39). Note that the convergence of the predictions of the hole area is achieved approximately after 11 sec of diagnostics.

The mean values and standard deviations of the parameters $\{a_i\}$ reconstructed during diagnostics can now be used to integrate model of internal ballistics forward in time to obtain predictions of the pressure and thrust dynamics in the presence of the fault. The

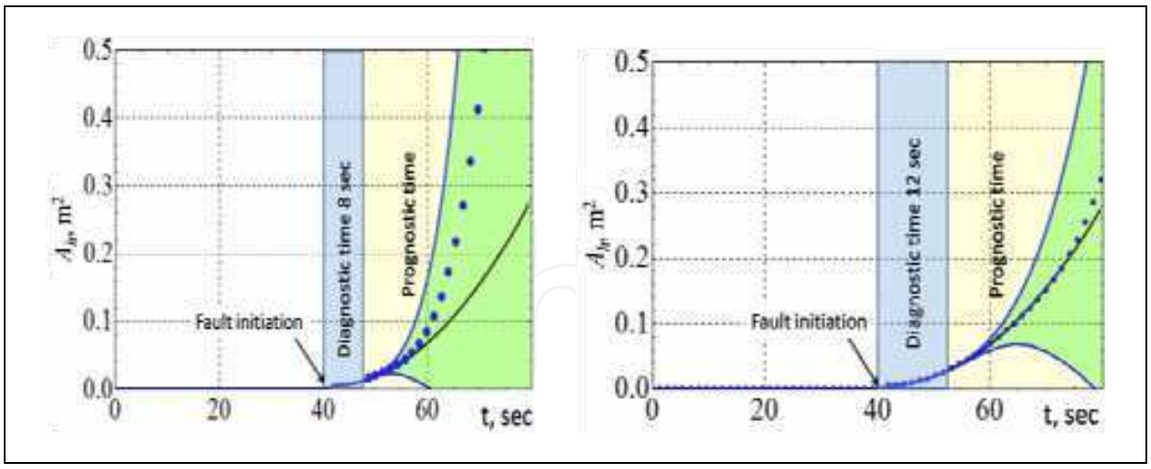

Fig. 14. Prognostic of the case breach area. The actual time series of the fault area $A_h(t)$ are shown by black lines. The mean values of predicted dynamics of the $A_h(t)$ are shown by blue dotted lines for two different values of the diagnostic time-window: (i) 8 sec (left); (ii) 12 sec (right). The green shaded areas bounded by blue lines indicate standard deviation of the predictions. The blue shading indicates the time used for diagnostic of the fault parameters. The yellow shaded region indicates the prediction time.

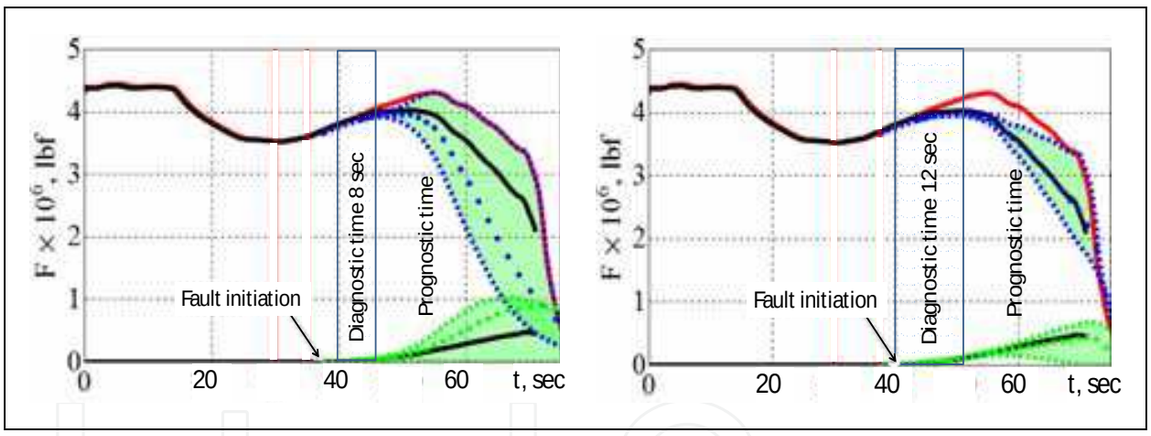

Fig. 15. The thrust in the nominal regime is shown by solid red line. The actual fault-induced time-traces of thrust are shown by black lines. The time-traces of mean predicted values of the thrust are shown by blue dots. The predicted values of the nozzle thrust and the side thrust are indicated by green shading bounded by blue dotted lines and green dotted lines respectively. In the figures the prediction is made after ΔT_m=8 sec (left) and ΔT_m=12 sec (right).

results of the predictions for the nozzle and side thrust are shown in the Fig. 15. In this test the fault was located at the middle of the motor and initial time T_f = 40 sec. The hole radius growth rate is 0.3 in/sec. We take the initial radius of the hole equal to 0.1in. It can be seen that convergence is achieved after approximately 12 sec of diagnostics time.

We conclude that the model (34) allows for accurate calculations of the internal ballistics of SRMs in nominal and off-nominal regimes. This model can further be applied for development of the FD&P system of the case breach fault as discussed in this and previous

sections. We also note that many SRMs fault modes including e.g. nozzle blocking, bore choking, and propellant cracking can be related to the changes in the grain and/or nozzle geometry at a particular section of the SRM. Therefore these changes can be conveniently modeled using (34) and by introducing corresponding modifications into the grain geometry equations (8) and (9) in the form of additional time-dependent fault terms

$$A_p(x_i) = f_{Ai}(R(x_i)) + A_{p,fault}(t), \quad l(x_i) = f_{li}(R(x_i)) + l_{fault}(t). \tag{41}$$

The dynamics of these fault modes can be based on the corresponding failure physics (cf. with the model of the case breach in Sec. 2.4) or modeled by parametric equation similar to Eq. (39). The corresponding FD&P systems for the propellant cracking and nozzle blocking faults can be based on the algorithms similar to one discussed in this chapter.
We now briefly outline the procedures of V&V used to verify and validate the results obtained for the case breach fault.

5.4 Validation and verification of the FD&P system

The practical application of the FD&P algorithms requires extended V&V procedure that may take 80% and more of the total development time. The V&V of the case breach and nozzle blocking models was performed in a number of stages. The results of simulations for large motor were compared with the results of high-fidelity simulations obtained using direct integration of the model equations (Smelyanskiy et al., 2006). For a sub-scale motor the results of the simulations were verified using high-fidelity FLUENT non-stationary model (Osipov et al., 2007; Luchinsky et al., 2008) as is described in Sec. 3.3. Next the FD&P system was validated using analysis of the results of the ground firing test of a subscale motor (Smelyanskiy, 2008a & 2008b). In this section we briefly discuss verification of the FD&P system for a large segmented motor by comparison the results of prediction of the fault dynamics obtained using model (34) with the results of calculations of the fault dynamics using scaling algorithm (McMillin, 2006). This scaling algorithm (McMillin, 2006), unlike FD&P algorithm presented above, requires a knowledge of the time-trace of the pressure in the nominal regime. Since this requirement is a necessary prerequisite for the space flight one can substantially reduce the prediction time. Let us remind briefly main steps of the scaling algorithm (McMillin, 2006). The key assumption based on extensive experimental results is that the empirical coefficient q

$$q = \frac{\partial \ln(C^*)}{\partial \ln(p)} = const, \qquad C^* = \frac{p^{1-n} A_t}{A_b \rho_p a}. \tag{42}$$

is constant. Here $C^* = pA_t / \dot{m}$ is characteristic exhaust velocity and $\dot{m} = A_b \rho_p \dot{R} = A_b \rho_p a p^n$ is the mass flow with total burning area A_b, where the burning law is given by $\dot{R} = ap^n$. To see more clearly the meaning of (42) we write its solution on a discrete time lattice $\{t_i: i=1,\ldots,N\}$ chosen in such a way that every moment of time in the nominal t_{Ni} and off-nominal t_{Di} regimes corresponds the same fixed lattice of burned distances $\{r_i: i = 1,\ldots,N\}$ and therefore the burning area $A_{b,i}$ at any given instant of time is also the same

$$C_i^* p_i^{-q} = \frac{p_i^{1-n-q} A_{t,i}}{A_{b,i} \rho_p a} = const \tag{43}$$

The experiments and numerical simulation show that the later expression is constant with good accuracy during the steady burn out of the propellant both in nominal (*N*) and off-nominal, deviant (D), regimes. We notice that the mean value of q is approximately 0.007, i.e. 2 orders of magnitude less than (1-n) = 0.7 and can be neglected in the calculations.
Using Eq. (43) for the nominal p_{Ni} and off-nominal p_{Di} pressures at the instant t_i on a given time lattice $\{t_i\}$ we obtain

$$p_{Di} = p_{Ni} \left(A_{t,Ni} / A_{t,Di} \right)^{\frac{1}{1-n-q}}, \tag{44}$$

where $A_{t,Ni}$ and $A_{t,Di}$ are nozzle throat area in the nominal regime and the nozzle effective area in the off-nominal regime at the instant t_i on the nominal time lattice $\{t_i\}$ and instant t_{Di} on the deviant time lattice $\{t_{Di}\}$. It was noticed that if the lattice of burned distances $\{r_i\}$ is kept the same in nominal and off-nominal regimes the corresponding time lattices $\{t_i\}$ in these two regimes will be different. To find the scaling of the time lattice the burning law is used as follows (McMillin, 2006)

$$\Delta r_i = r_i - r_{i-1} = a p_{Ni}^n \Delta t_{Ni} = a p_{Di}^n \Delta t_{Di}$$

or

$$\Delta t_{Di} = \Delta t_{Ni} \left(p_{Ni} / p_{Di} \right)^n. \tag{45}$$

Therefore, the time scale in the presence of the fault is

$$t_{D,i} = t_{D,i-1} + \Delta t_{Di}. \tag{46}$$

Finally, substituting (44) into (45) we have

$$\Delta t_{Di} = \Delta t_{Ni} \left(A_{t,Ni} / A_{t,Di}^e \right)^{\frac{-n}{1-n-q}}. \tag{47}$$

Fault dynamics can be given in any form, in particular it is a given function of time (McMillin, 2006)

$$A_{h,i} = f(t_{D,i} - t_f). \tag{48}$$

The effective nozzle throat area for the case breach fault $A^e_{t,D}$ is the sum of the hole area A_h in the case and of the slightly modified nozzle throat area $A_{t,D}$

$$A_{tD,i}^e = A_{h,i} + A_{tD,i}. \tag{49}$$

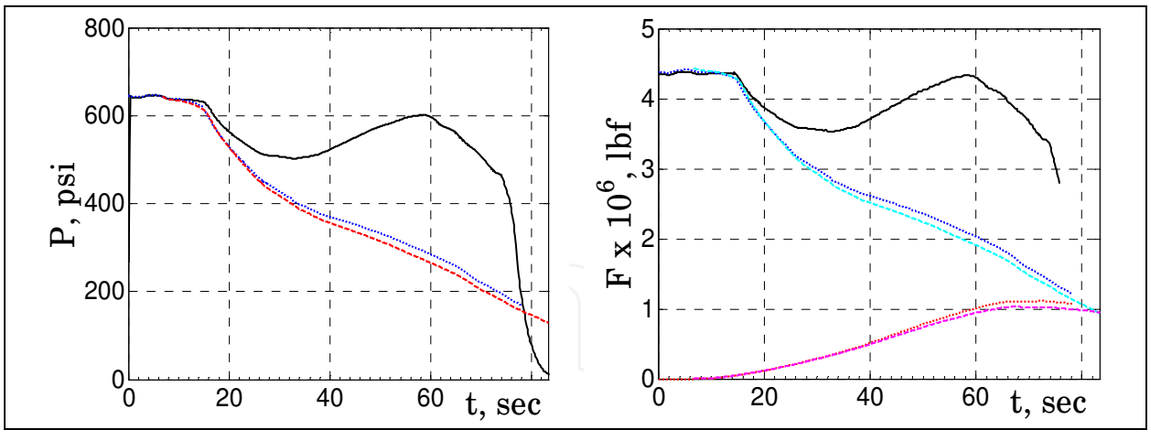

Fig. 16. (left) Nozzle pressure (black line) in the nominal regime is compared with the calculations of the fault induced pressure using 1D model (blue dotted line) and scaling algorithm (red dashed line). (right) Nozzle vacuum thrust (black line) in the nominal regime as compared to the deviation of the thrust from nominal regime calculated using scaling algorithm (cyan dashed line) and 1D calculations (blue dotted line). The time-traces of the hole' thrust calculated using scaling equations and 1D algorithm are shown by magenta dashed line and red dotted line respectively.

To calculate nozzle thrust the empirical constant thrust coefficient was used

$$C_F = F_N / pA_{t,N}, \qquad C_{F,N} = C_{F,D}. \tag{50}$$

If combined with (44) the following result for the deviant nozzle thrust F_{Di} can be obtained

$$F_{Di} = F_{Ni} = \left(\frac{A_{t,Di}}{A_{t,Ni}}\right)\left(\frac{A_{t,Ni}}{A^e_{t,Di}}\right)^{\frac{1}{1-n-q}}. \tag{51}$$

Eq. (51)can be used to calculate the side breach thrust. The resulting expression for the side vacuum thrust (p_{amb} = 0) can be simplified

$$F_h = p_0 A_h \left(\frac{2}{\gamma+1}\right)^{\frac{\gamma}{\gamma-1}}(\gamma+1). \tag{52}$$

The algorithm suggested in earlier work (McMillin, 2006) consists of iteration of Eqs. (46)-(49) until convergence of Δt_i is achieved. On substituting Eq. (48) into Eq. (49) and Eq. (49) into Eq. (47) the equations. (46)-(49) can be reduced to two equations in the form

$$\Delta t_{Di} = \Delta t_{Ni}\left(\frac{A_{t,i}}{A_{tD,i} + f(t_{D,i} - t_f)}\right)^{\frac{-n}{1-n-q}}, \quad t_{D,i} = t_{D,i-1} + \Delta t_{Di}. \tag{53}$$

where t_{Di} is given by (46). There are three unknown variables $\{\Delta t_{Di}, A_{tDi}, t_{Di}\}$ in two Eqs. (53), therefore one more equation is needed to implement iterative procedure. We use assumption (McMillin, 2006) that the nozzle throat area is only a function of time $A_{tD}(t_{Di}) = A_{tN}(t_{Di})$, which holds for actual rocket parameters.

We now verify both algorithms by direct comparison of their performance in off-nominal regime with the fault initial time 10 sec and initial hole radius 0 in. The results of the calculation of pressure, nozzle and side thrusts using model integration and scaling equations are shown in the Fig. 16. It is clear from the figure that the numerical integration of the model and the results of predictions based on the scaling equations are in good agreement. The maximum relative deviation of the scaling algorithm results from the results of simulations is less than 7%. Note that the safety margins do not allow for the deviation of the nozzle thrust more than 10% of the nominal regime. Within these safety margins the agreement between the predictions based on the scaling algorithm results and on simulations is better than 1%. The reason for the small deviation of the scaling algorithm from the results of integration of the model is that the scaling algorithm overestimates nozzle throat ablation, while chamber pressure and nozzle thrust are slightly underestimated. The nozzle ablation modeling in the scaling algorithm will be improved in the next version of the code.

5.5 Application to the calculation of the flight safety envelopes

In this section we describe one of the applications of the case breach model in large segmented SRMs. Objective of this application is to study response of the TVC of a large segmented motor to side thrust torque and compute at which moment the vehicle will leave the flight safety window. We introduce the flight safety window in the following way: altitude difference between the flight with the side thrust and the nominal flight is not larger than 4000 ft; the vehicle's angle of attack for the flight with the side thrust is in +20/-20 degrees interval. We assume that the flight is not safe if the rocket has altitude difference larger than altitude difference margin (4000 ft) or if the angle of attack of the rocket is larger than 20 degrees in absolute value. We assume that the side thrust appears at forward and aft field joints at 0, 90, 180 and 270 degrees angle location at times from 0 to 120 seconds with 5 second interval. We use the model (34) to calculate nozzle and side thrusts, and the gas flow rate in the combustion chamber. The results of these calculations were fed into special purpose software to calculate rocket trajectory taking into account TVC. The simulations were performed about 200 times for different breach locations and different times. The breach radius growth rate for these simulations was taken 0.3 in/sec. The flight time safety envelopes were created by plotting nominal flight times against the side thrust start times for given joint position and breach location angle.

The side thrust safety envelopes were created by plotting the side thrust profiles against the side thrust start times for given joint position and breach location angle. The regions of failure were determined by plotting points of failure for each flight trajectory. It was found that for 0, 180 degrees breach location the rocket loses control due to rapid change of the altitude, for 90, 270 degrees breach location the rocket loses control mostly due to oscillations of the angle of attack. In Fig. 17 we present the flight time safety envelopes for forward and aft field joints at 0 degree angle location. The areas under the black curves restrict regions of nominal vehicle flights, while the areas outside these curves correspond to the faulty flights.

The side thrust safety envelopes describing values of side thrusts for forward and aft field joints with 0 and 90 degrees of breach locations are shown in Fig. 18. The results for 180 and 270 degrees breach locations are similar to the results for 0, 90 degrees.

The blue areas in these plots correspond to side thrusts for the nominal flights and the red areas correspond to the faulty flights. As follows from these plots, the areas of blue regions of the envelopes are more sensitive to joint location for 0 degree breach location, but still the same for 90 degrees breach locations.

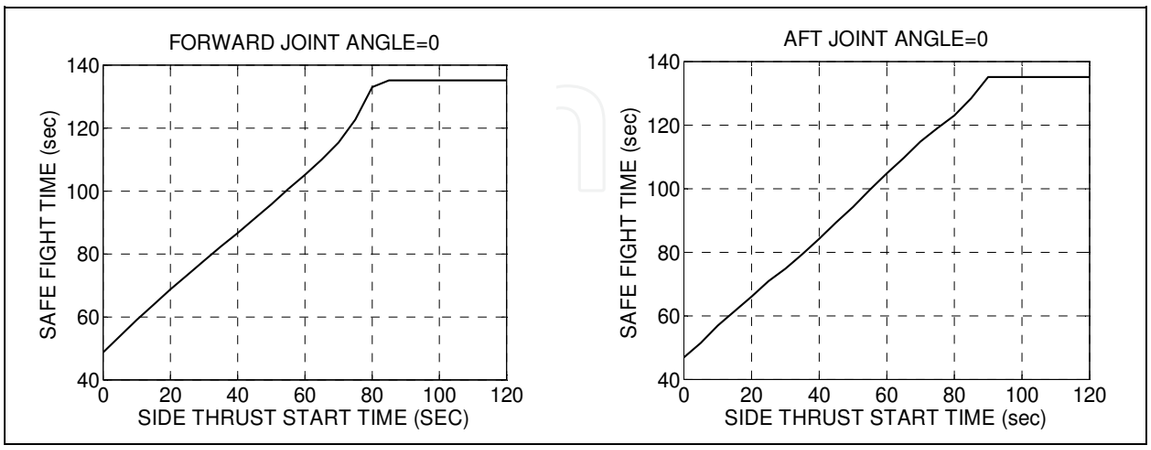

Fig. 17. The left plot corresponds to the flight time safety envelope for forward joint and the right plot corresponds to the flight time safety envelope for the aft joint at 0 deg breach location.

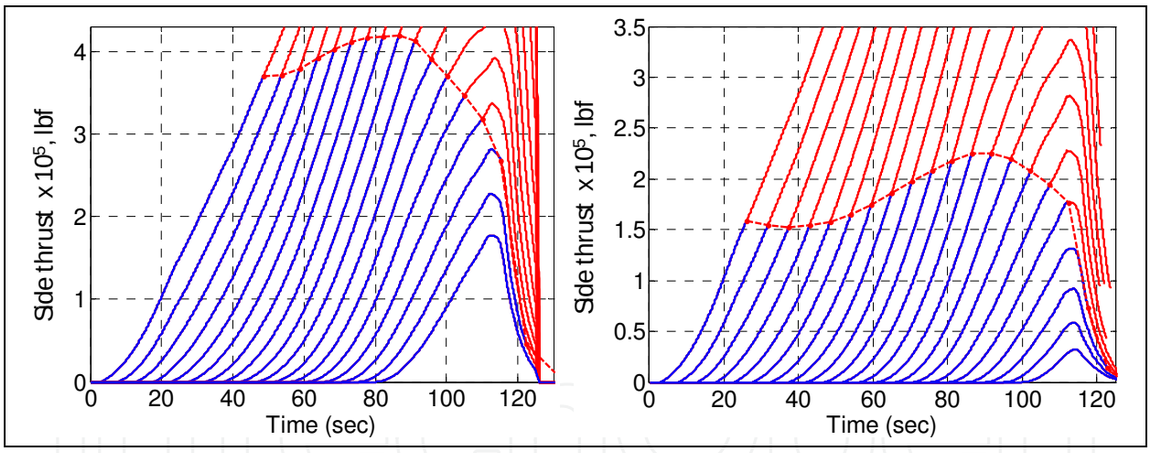

Fig. 18. (left) Side thrust values for 2nd joint, 0 deg breach location. (right) Side thrust values for 5th joint , 90 deg breach location. X-axis is start time of the side thrust. The hole radius growth rate was 0.3 in/sec.

6. Conclusion

In this chapter we report the work in progress on the development of hybrid probabilistic algorithms for SRMs on-board IVHM system. We introduce model that describe accurately internal ballistic of SRM in nominal and off-nominal regime. The model is verified by comparison with the results of high-fidelity simulations. A number of algorithms are derived to infer fault parameters and to predict fault dynamics. The algorithms

accommodate abrupt changes in the model parameters and can be used to develop hybrid probabilistic on-board SRM IVHM. The performance of the algorithms was tested using analysis of the experimental time-series data. It is shown that the algorithm can be successfully applied for the prognostics of the case breach fault. The model is used to develop on-board FD&P of the case breach fault and applied to predict fault-induced internal ballistics of a large segmented SRM.

The developed methods and algorithms can be used to analyze other SRM' faults, including overpressure and breakage of the case induced by nozzle blocking, bore choking and grain deformation. The bore choking phenomenon is an almost radial deformation (bulge) of the propellant near booster joint segments. This phenomenon can cause choking of the exhaust gas flow and increase the burning surface which can lead to critical overpressure in the combustion chamber. Development testing has shown that this fault was observed, for example, in primary construction of the Titan IV (Coats, 2003; Wilson, 1992). The bore choking, and also cracks and voids in the solid propellant, can result in local burning of the booster case and also in abrupt breaking off of large pieces of the propellant. These pieces can stick in the nozzle throat and block the exhaust gas flow (nozzle blocking fault). In all these cases the fault dynamics is governed by the changes in the burning area and/or effective nozzle area. Therefore the model introduced in this work can be efficiently applied to the analysis of these faults and development of the on-board FD&P.

7. Nomenclature

ρ	=	gas density
p	=	gas pressure
T	=	gas temperature
u	=	gas velocity
ρ_p	=	density of the solid propellant
H	=	combustion heat of the solid propellant
e_T	=	total energy of the gas
h_T	=	total enthalpy of the gas
c_p	=	specific heat for the constant pressure
c_V	=	specific heat for the constant volume
γ	=	ration of specific heats $\gamma = c_P/c_V$
A_p	=	port area (cross-sectional area of combustion chamber)
A_h	=	hole port area
A_b	=	burning area of the propellant
r_b	=	burning rate of solid propellant
R	=	thickness of the burned propellant layer
$\dot{r}_{er}$	=	erosive burning rate of solid propellant
T_{abl}	=	critical temperature of the nozzle ablation
q_{ins}	=	latent heat of insulator ablation
c	=	sound velocity
M	=	Mach number, $M = u/c$
F_N	=	normal thrust

F_h	=	additional thrust produced by hole gas flow
Q	=	heat flow from the gas to the walls of the hole
Q_c	=	heat flow due to convection
Q_R	=	heat flow due to radiation
Q_b	=	heat flow due to burning
v_{t0}	=	velocity of the ablation of the nozzle throat
c_{ins}	=	heat capacity of the insulator
q_{met}	=	specific melting heat of the metal case
ρ_{met}	=	metal density
T_{met}	=	metal temperature
C_{met}	=	heat capacity of the metal case
λ	=	the emissivity of the hot gas
v_{fb}	=	velocity of the burning front propagation
V	=	volume of the combustion chamber
in	=	subscript for parameters of the insulator
ex	=	subscript for parameters at the nozzle exit
h	=	subscript for gas parameters in the hole
t	=	subscript for gas parameters in the nozzle and hole throat
N	=	subscript for parameters in normal regime
0	=	subscript for stagnation values of gas parameters

8. References

Bartz, D.R. (1965). Heat Transfer from Rapidly and from Heated Air, in Advances in Heat Transfer, vol. 2, Hartnett, J. P., and Irvine, T. F. Jr., eds., New York: Academic Press.

Dick, W. A. et al. (2005, July). Advanced Simulation of Solid Propellant Rockets from First Principles", Center for Simulation of Advanced Rockets, University of Illinois, in Proceeding of 41st AIAA Joint Propulsion Conference & exhibit, Tucson, Arizona.

Congdon, P. (2001). “Bayesian statistical modelling”, Wiley series in probability and statistics (Wiley, Chichester).

Coats, D.E.; Dunn, S.S. & French, J.C. (2003) “Performance Modeling Requirements for Solid Propellant Rocket Motors”, 39th JANNAF Combustion Subcommittee, Colorado Springs, CO, December.

Culick, F. E. C. (1974). “Stability of Three-Dimentional Motions in a Rocket Motor”, Combustion and Technology, v. 10, 109.

Culick, F. E. C. & Yang, V. (1992). Prediction of the Stability of Unsteady Motions in Solid Propellant Rocket Motors, Nonsteady Burning and Combustion Stability of Solid Propellants, edited by L. De Luca, E. W. Price, and M. Summerfield, Vol. 143, Progress in Astronautics and Aeronautics, AIAA, Washington, DC, pp. 719–779.

Culick, F. E. C. (1996). Combustion of the Stability in Propulsion Systems, Unsteady Combustion, Kluwer Academic Publisher.

Dykman, M. I. (1990). “Large fluctuations and fluctuational transitions in systems driven by colored Gaussian noise -- a high frequency noise”, Phys. Rev. A, Vol. 42, 2020—2029.

Graham, R. (1973). paper in Quantum Statistics in Optics and Solid-State Physics, edited by G. Höhler, Springer-Verlag, Berlin, vol. 66, Chap. 1, p. 1.

Graham, R. (1977). "Path Integral Formulation Of General Diffusion Processes", Z. Phys. B, Vol. 26, 281-290.

Flandro, G. A. et al. (2004). "Nonlinear Rocket Motor Stability Prediction: Limit Amplitude, Triggering, and Mean Pressure Shift", in Proceeding of AIAA 2004-4054, 40th AIAA Joint Propulsion Conference & Exhibit, July, 2004, Florida.

Flandro, G. A. (1982). Approximate Analysis of Nonlinear Instability with Shock Waves, AIAA-82-120, 18th AIAA Joint Propulsion Conference, June, 1982, Ohio.

Knoll, D.A.; Chacon, L.; Margolin, L.G. & Mousseau, V.A. (2003). On balanced approximations for time integration of multiple time scale systems", J. Comput. Phys., 185(2), pp 583-611.

Hill, P. & Peterson, C. (1992). Mechanics and Thermodynamics of Propulsion, 2-rd ed., Addison-Wesley Publishing Company, Inc. New York.

Handbook of Heat Transfer Application. (1973), 2-rd ed,

Jeffreys, H. (1961). Theory of Probability, 3-rd ed. (Clarendon Press, Oxford).

Incropera, F.P. & DeWitt, D. P. (2002). Introduction to Heat Transfer, John Wiley & Sons, NY.

Isaac, D. A. & Iverson, M.P. (2003), "Automated Fluid-Structure Interaction Analysis", ATK Thiokol Propulsion, A Division of ATK Aerospace Company. L. D. Landay and E. M. Lifshits. (1987), Fluid Mechanics (Pergamon).

Luchinsky, D.G.; Millonas, M.M.; Smelyanskiy, V.N.; et al. (2005). "Nonlinear statistical modeling and model discovery for cardiorespiratory data". Phys. Rev. E, Vol. 72, 021905.

Luchinsky, D.G.; Smelyanskiy, V.N.; Osipov, V.V.; Timucin, D. A. & Lee, S. (2007). "Data management and decision support for the in-flight SRM", in Proceeding of AIAA-2007-2829 AIAA Infotech@Aerospace 2007 Conference and Exhibit, Rohnert Park, , May, California.

Luchinsky, D.G.; Osipov, V.V.; Smelyanskiy, V.N.; Timucin, D.A. & Uckun, S. (2008), "Model based IVHM system for the solid rocket booster " in Proceeding of Aerospace Conference, 2008 IEEE, 1-8, March, BigSky, Montana, Page(s):1 – 15.

Luchinsky, D.G.; Osipov, V.V.; Smelyanskiy, V.N.; Timucin, D.A.; Uckun, S.; Hayashida, B.; Watson, M.; McMillin, J.; Shook, D.; Johnson, M. & Hyde, S. (2009), "Fault Diagnostics and Prognostics for Large Segmented SRMs", in Proceeding of 2009 IEEE Aerospace Conference, Big Sky, March, Montana.

McMillin, J.E. (2006, July). AIAA 2006-5121, in Proceeding of 42nd AIAA/ASME/ SAE/ASEE Joint Propulsion Conference & Exhibit , Sacramento, CA.

Oberg, J. (2005). ''Deadly space lessons go unheeded'', NBC News, http://www.mission511.com/disaster.htm

Osipov, V. V. ; Luchinsky, D. G.; Smelyanskiy, V.N.; Lee, S.; Kiris, C. & Timucin, D. (2007, March), "Bayesian Framework for In-Flight SRM Data Management and Decision Support", in Proceeding of IEEE 2007 Aerospace Conference, Big Sky.

Osipov, V.V.; Luchinsky, D.G.; Smelyanskiy, V.N.; Kiris, C.; Timucin, D.A. & Lee. S.H. (2007, July), In-Flight Failure Decision and Prognostic for the Solid Rocket Buster, in

Proceeding of AIAA-2007-5823, 43rd AIAA/ASME/SAE/ ASEE Joint Propulsion Conference and Exhibit, Cincinnati, OH, July.

Rhsenow, W. M.; Hartnett, J. P. & Ganic, E. N. (1973), McGraw-Hill Book Company, New York

Rogers (1986). Rogers Commission report. Report of the Presidential Commission on the Space Shuttle Challenger Accident.

Risfic, B.; Arulampalam, S. & Gordon, N. (2004), "Beyond the kalman filter - Book Review ", Aerospace and Electronic Systems Magazine, IEEE, Vol. 19, No. 7, 37- 38.

Sailta, M. (1989, January). "Verification of Spatial and Temporal Pressure Distribution in Segmented Solid Rocket Motors," in Proceeding of AIAA paper 89-0298, 27th Aerospace Science Meeting, Reno, Nevada.

Salita, M. (2001). "Modern SRM ignition transient modeling. I - Introduction and physical models", in Proceeding of AIAA-2001-3443, AIAA/ASME/SAE/ASEE Joint Propulsion Conference and Exhibit, 37th, Salt Lake City, U.

Salita, M. (1989, July). "Closed-Form Analytical Solutions for Fluid Mechanical, Thermochemical, and Thermal Processes in Solid Rocket Motors", in Proceeding of AIAA 98-3965, 34th Joint Propulsion Conference, Cleveland.

Santiago, J.C. (1995), "An experimental study of the velocity field of a transverse jet injected into a supersonic crossflow", Ph.D. thesis, University of Illinois, Urbana-Champaign.

Shapiro, A.H. (1953.), "The Dynamics and Thermodynamics of Compressible Fluid Flow", Ronald Press, NY, vol. I.

Sorkin, E. (1967), Dynamics and Thermodynamics of Solid-Propellant Rockets, Wiener Bindery Ltd., Jerusalem.

Smelyanskiy, V. N., D. G. Luchinsky, D. A. Timuçin, and A. Bandrivskyy. (2005a), "Reconstruction of stochastic nonlinear dynamical models from trajectory measurements", Phys.l Rev. E, Vol. 72, 026202.

Smelyanskiy, V. N.; Kiris, C.; Osipov, V. V.; Luchinsky, D. G.; Timucin, D. A.; & Uckun, S. (2006). "Solid Rocket Motor Health Management for Safe Space Flight", in Proceeding of AIAA Guidance, Navigation, and Control Conference and Exhibit, Keystone, Colorado. August.

Smelyanskiy, V.N.; Luchinsky, D.G.; Osipov, V.V.; Timucin, D.A.; Uckun, S.; Hayashida, B.; Watson, M.; McMillin, J.; Shook, D.; Johnson, M. & Hyde, S. (2008a), "Analysis of experimental time-traces of the ground firing test of a subscale SRM with gas leak in the forward closure", in Proceeding of 6th Modeling and Simulation/4th Liquid Propulsion/3rd Spacecraft Propulsion Joint Subcommittee Meeting, Orlando, December Florida.

Smelyanskiy, V.N.; Luchinsky, D.G.; Osipov, V.V.; Timucin, D.A.; Uckun, S.; Hayashida, B.; Watson, M.; McMillin, J.; Shook, D.; Johnson, M. & Hyde, S. (2008b) "Fault diagnostic and prognostic system for a gas leak fault in subscale SRM: modelling and verification in a ground firing test", 6th Modeling and Simulation / 4th Liquid Propulsion / 3rd Spacecraft Propulsion Joint Subcommittee Meeting, Orlando, December Florida.

Smelyanskiy, V.N.; Luchinsky, D.G.; Osipov, V.V.; Timuchin, D.A. & Uckun, S. (2008c), "Development of an on-board failure diagnostics and prognostics system for Solid Rocket Booster", in Proceeding of 44rd AIAA/ASME/SAE/ASEE Joint Propulsion Conference & Exhibit, Hartford, CT.

Hathout, J.P.; Fleifil, M.; Annaswamy, A.M. & Ghoniem, A.F. "Active control of combustion instability using fuel-injection in the presence of time-delays," AIAA J. Propulsion and Power, vol. 18, no. 2, pp. 390-399, 2002.

Stewart, D.S.; Tang, K.C.; Yoo, S.; Brewster, Q. & Kuznetsov, I.R.. (2006). Multiscale Modeling of Solid Rocket Motors: Computational Aerodynamic Methods for Stable Quasi-Steady Burning, Journal of Prop and Power, Vol. 22, no. 6, 1382-1388.

Wilson, W.G.; Anderson, J. M. & Vander Meyden, M. (1992). "Titan IV SRMU PQM-1 Overview", AIAA paper 92-3819, in Proceeding of AIAA/SAE/ASME/ASEE, 28th Joint Propulsion Conference and Exhibi, Nashville, TN.

Young, S.; Bruck, G. & Gowrisankaran, S. (2003). "Modeling of Rocket Motor Ballistics for Functionally Graded Propellants", Proceedings of the 39th JANNAF Combustion Meeting, Colorado Springs, CO, December.

IntechOpen

Aerospace Technologies Advancements

Edited by Thawar T. Arif

ISBN 978-953-7619-96-1

Hard cover, 492 pages

Publisher InTech

Published online 01, January, 2010

Published in print edition January, 2010

Space technology has become increasingly important after the great development and rapid progress in information and communication technology as well as the technology of space exploration. This book deals with the latest and most prominent research in space technology. The first part of the book (first six chapters) deals with the algorithms and software used in information processing, communications and control of spacecrafts. The second part (chapters 7 to 10) deals with the latest research on the space structures. The third part (chapters 11 to 14) deals with some of the latest applications in space. The fourth part (chapters 15 and 16) deals with small satellite technologies. The fifth part (chapters 17 to 20) deals with some of the latest applications in the field of aircrafts. The sixth part (chapters 21 to 25) outlines some recent research efforts in different subjects.

How to reference

In order to correctly reference this scholarly work, feel free to copy and paste the following:

D.G. Luchinsky, V.V. Osipov, V.N. Smelyanskiy, I. Kulikov, A. Patterson-Hein, B. Hayashida, M. Watson, D. Shook, M. Johnson, S. Hyde and J. Shipley (2010). Integrated Vehicle Health Management for Solid Rocket Motors, Aerospace Technologies Advancements, Thawar T. Arif (Ed.), ISBN: 978-953-7619-96-1, InTech, Available from: http://www.intechopen.com/books/aerospace-technologies-advancements/integrated-vehicle-health-management-for-solid-rocket-motors

INTECH
open science | open minds

InTech Europe
University Campus STeP Ri
Slavka Krautzeka 83/A
51000 Rijeka, Croatia
Phone: +385 (51) 770 447
Fax: +385 (51) 686 166
www.intechopen.com

InTech China
Unit 405, Office Block, Hotel Equatorial Shanghai
No.65, Yan An Road (West), Shanghai, 200040, China
中国上海市延安西路65号上海国际贵都大饭店办公楼405单元
Phone: +86-21-62489820
Fax: +86-21-62489821

© 2010 The Author(s). Licensee IntechOpen. This chapter is distributed under the terms of the Creative Commons Attribution-NonCommercial-ShareAlike-3.0 License, which permits use, distribution and reproduction for non-commercial purposes, provided the original is properly cited and derivative works building on this content are distributed under the same license.

IntechOpen

IntechOpen